GERDA

Progress report to the LNGS scientific committee

(Appendix)

LNGS-EXP 33/05 add. 9/09

This GERDA report summarizes the progress achieved during the last six months. A *Short Write-up* is linked at

`http://www.mpi-hd.mpg.de/GERDA/reportsLNGS/gerda-lngs-sc-nov09-shwup.pdf`.

Experimental and technical details are given in the *Appendix* which is linked at

`http://www.mpi-hd.mpg.de/GERDA/reportsLNGS/gerda-lngs-sc-nov09-appdx.pdf`.

Previous reports are available at `http://www.mpi-hd.mpg.de/GERDA/reportsLNGS`.

November 2009

M. Allardt [c], A.M. Bakalyarov [l], M. Balata [a], I. Barabanov [j], M. Barnabe-Heider [f], L. Baudis [q], C. Bauer [f], E. Bellotti [g,h], S. Belogurov [k,j], S.T. Belyaev [l], A. Bettini [n,o], L. Bezrukov [j], F. Boldrin [n,o], V. Brudanin [d], R. Brugnera [n,o], D. Budjas [f], A. Caldwell [m], C. Cattadori [g,h], E.V. Demidova [k], A. Denisiv [j], A. Di Vacri [a], A. Domula [c], A. D'Andragora [a], V. Egorov [d], A. Ferella [q], F. Froborg [q], N. Frodyma [b], A. Gangapshev [j], A. Garfagnini [n,o], S. Gazzana [f], A. Glück [m], R. Gonzalea de Orduna [e], P. Grabmayr [p], G.Y. Grigoriev [l], K.N. Gusev [l,d], V. Gutentsov [j], A. Hagen [p], W. Hampel [f], M. Heisel [f], G. Heusser [f], W. Hofmann [f], M. Hult [e], L.V. Inzhechik [l], J. Janicsko [m], M. Jelen [m], J. Jochum [p], M. Junker [a], S. Kionanovsky [j], I.V. Kirpichnikov [k], A. Klimenko [d,j], M. Knapp [p], K-T. Knoepfle [f], O. Kochetov [d], V.N. Kornoukhov [k,j], V. Kusminov [j], M. Laubenstein [a], V.I. Lebedev [l], D. Lenz [m], S. Lindemann [f], M. Lindner [f], I. Lippi [o], J. Liu [m], X. Liu [m], B. Lubsandorzhiev [j], B. Majorovits [m], G. Marissens [e], G. Meierhofer [p], I. Nemchenok [d], S. Nisi [a], L. Pandola [a], K. Pelczar [b], A. Pullia [i], S. Riboldi [i], F. Ritter [p], C. Rossi Alvarez [o], R. Santorelli [q], J. Schreiner [f], J. Schubert [m], U. Schwan [f], B. Schwingenheuer [f], S. Schönert [f], M. Shirchenko [l], H. Simgen [f], A. Smolnikov [d,j], L. Stanco [o], F. Stelzer [m], H. Strecker [f], M. Tarka [q], A.V. Tikhomirov [l], C.A. Ur [o], A.A. Vasenko [k], S. Vasiliev [d,j], M. Weber [f], M. Wojcik [b], E. Yanovich [j], S.V. Zhukov [l], F. Zocca [i], K. Zuber [c], and G. Zuzel [f].

[a]) INFN Laboratori Nazionali del Gran Sasso, LNGS, Assergi, Italy

[b]) Institute of Physics, Jagellonian University, Cracow, Poland

[c]) Institut für Kern- und Teilchenphysik, Technische Universität Dresden, Dresden, Germany

[d]) Joint Institute for Nuclear Research, Dubna, Russia

[e]) Institute for Reference Materials and Measurements, Geel, Belgium

[f]) Max Planck Institut für Kernphysik, Heidelberg, Germany

[g]) Dipartimento di Fisica, Università Milano Bicocca, Milano, Italy

[h]) INFN Milano Bicocca, Milano, Italy

[i]) Dipartimento di Fisica, Università degli Studi di Milano e INFN Milano, Milano, Italy

[j]) Institute for Nuclear Research of the Russian Academy of Sciences, Moscow, Russia

[k]) Institute for Theoretical and Experimental Physics, Moscow, Russia

[l]) Russian Research Center Kurchatov Institute, Moscow, Russia

[m]) Max-Planck-Institut für Physik, München, Germany

[n]) Dipartimento di Fisica dell'Università di Padova, Padova, Italy

[o]) INFN Padova, Padova, Italy

[p]) Physikalisches Institut, Eberhard Karls Universität Tübingen, Tübingen, Germany

[q]) Physik Institut der Universität Zürich, Zürich, Switzerland

Spokesperson: S. Schönert,
(Stefan.Schoenert@mpi-hd.mpg.de)
Co-Spokesperson: C. Cattadori
(Carla.Cattadori@lngs.infn.it)
Technical Coordinator: K.T. Knöpfle
(Karl-Tasso.Knoepfle@mpi-hd.mpg.de)
URL: http://www.mpi-hd.mpg.de/GERDA/reportsLNGS

Contents

1 Cryogenic vessel and infrastructure

During the last six months the cryostat installation was practically completed. The works included the vacuum infrastructure installation, mounting of the pipes for argon and nitrogen from the storage tanks to the LNGS ventilation duct, mounting of all safety devices including the argon gas - water heat exchanger and its connection to the LNGS cooling water system, cabling of all sensors and valves, and the installation of the PLC including the communication to the LNGS safety network. Not yet finished at the moment is the backup connection of the heat exchanger to the water tank. Fig. 1 shows some photos taken during the installation.

As far as possible the components passed a first commissioning test. These include reasonable readout values for all sensors, functioning of all valves, helium leak tests of all connections at the 10^{-9} mbar·l/sec range, functioning of safety interlocks of the PLC, alarm generations when sensors values passed their corresponding thresholds, pressure regulation of the cryostat, functioning of the alarm signal transmission to the LNGS safety system and their corresponding actions, and the verification that a large quantity of gas can be discharged through the pressure regulation system (about 300 m^3/h of warm gas through one valve for 300 mbar overpressure).

In addition, a so called radon shroud was installed. Its purpose was discussed in the previous report in section 11.2.2. The bottom part is a cylinder of 760 mm diameter and 3 m height made out of 30 μm thick copper foil (see Fig. 2). For the top part, the distance between the shroud and the crystals is more than 1.9 m. Hence, 1 mm thick stainless steel is used here. The shroud prohibits that convective liquid argon currents transport radon from the cryostat walls (location of radon sources) close to the diodes where it could decay and create background. A background reduction by a factor of 10 is expected if radon decays only outside of the 760 mm diameter cylinder. The copper foil was measured for its own radon emanation. Only an upper limit of 70 μBq was found for the area used, which is negligible compared to the emanation of the cryostat. With ICPMS, the bulk activity of the foil was measured to be smaller than 0.9 mBq/kg for ^{232}Th. Unfortunately, this limit is not very sensitive for our application.[1] In case of unforeseen problems, the copper part of the shroud can be cut without emptying the cryostat. The shroud is electrically isolated from the cryostat and can thus be put at positive or negative voltage. This might influence the background (see section 10).

The radon emanation of the cryostat was measured after the installation. The value of 55±4 mBq is about a factor of two higher than before and there is evidence that the emanation is higher in the neck of the cryostat (see section 10), i.e. the new sources could be located in some of the attached pipes. A detailed analysis of the individual emanation contributions is impracticable. Also, with the two active cooling circuits there should be very little mixing of the argon in the cryostat with the argon in the neck, since the latter will be tuned to a higher temperature. Therefore, radon from the neck (or from the connecting pipes) is not expected to get close to the diodes.

[1] For a typical copper value of <20 μBq/kg, the background index would be $2{\cdot}10^{-5}$ cts/(keV·kg·y).

The insulation vacuum pressure of the cryostat is now 10^{-5} mbar which is acceptable. An unexpected high outgasing rate is observed (10^{-3} mbar·l/sec currently) which is dominated by nitrogen. Our pumping speed is high enough to cope with this rate and if the observed decrease by a factor of 3 in one month continues, then we see no problem. After cooling down the cryostat, the situation should also improve.

A passive thermal insulation on the outside of the cryostat was added, see Fig. 3. It consists of a 6 mm thick layer of extruded polystyrol (brand name Jackodur) at the cylinder and bottom head of the cryostat. The plates were glued to the stainless steel and fixed afterwards by a plastic band and then covered with VM2000 foil. Any openings in the last layer were sealed by glueing to avoid water to penetrate under the insulation.

During November the cryostat will be cooled down and filled with liquid argon. As the last step the active cooling will be commissioned.

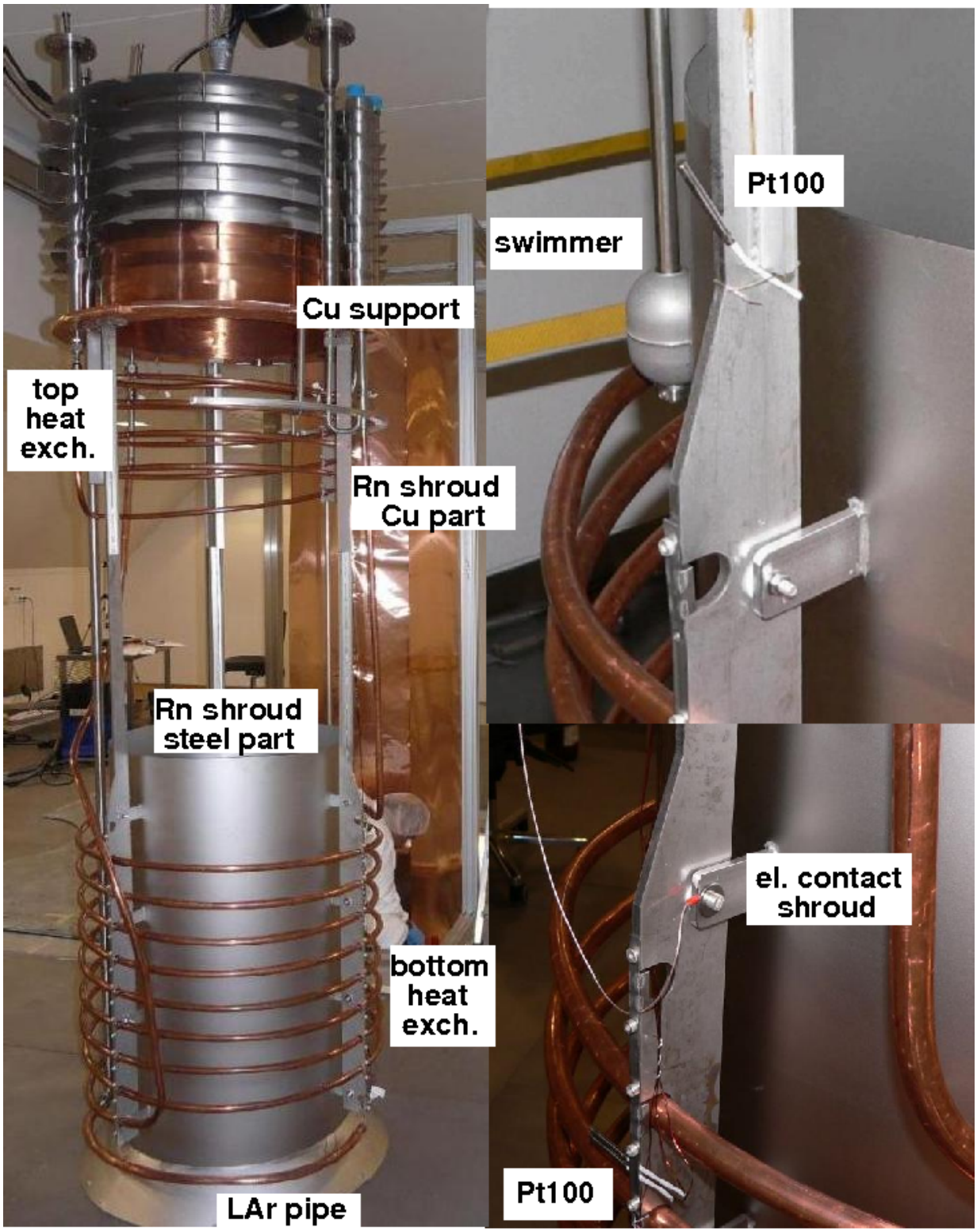

Figure 1: Pictures taken during the installation.

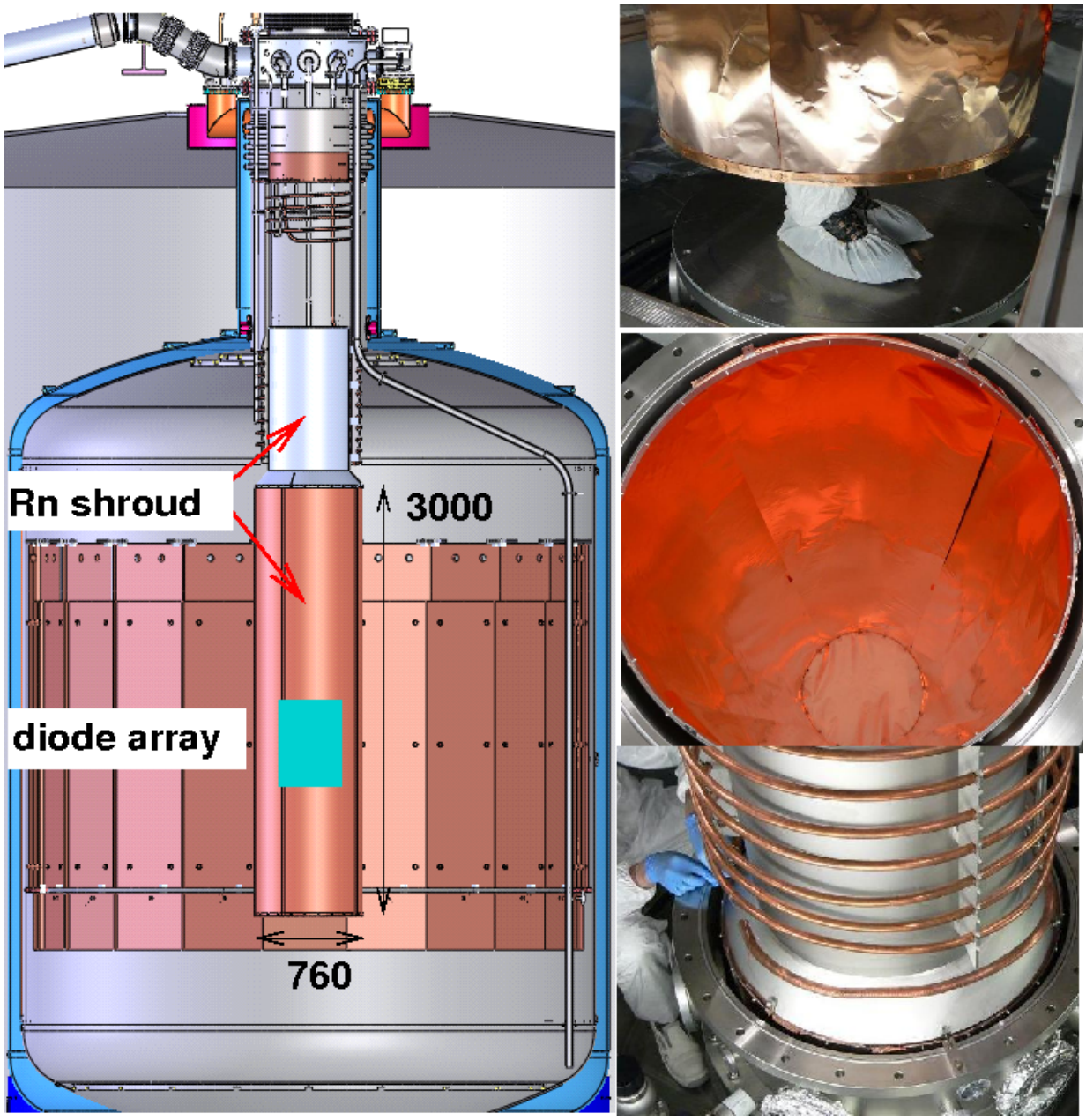

Figure 2: Left: cross section through the cryostat. Right: pictures taken during the installation.

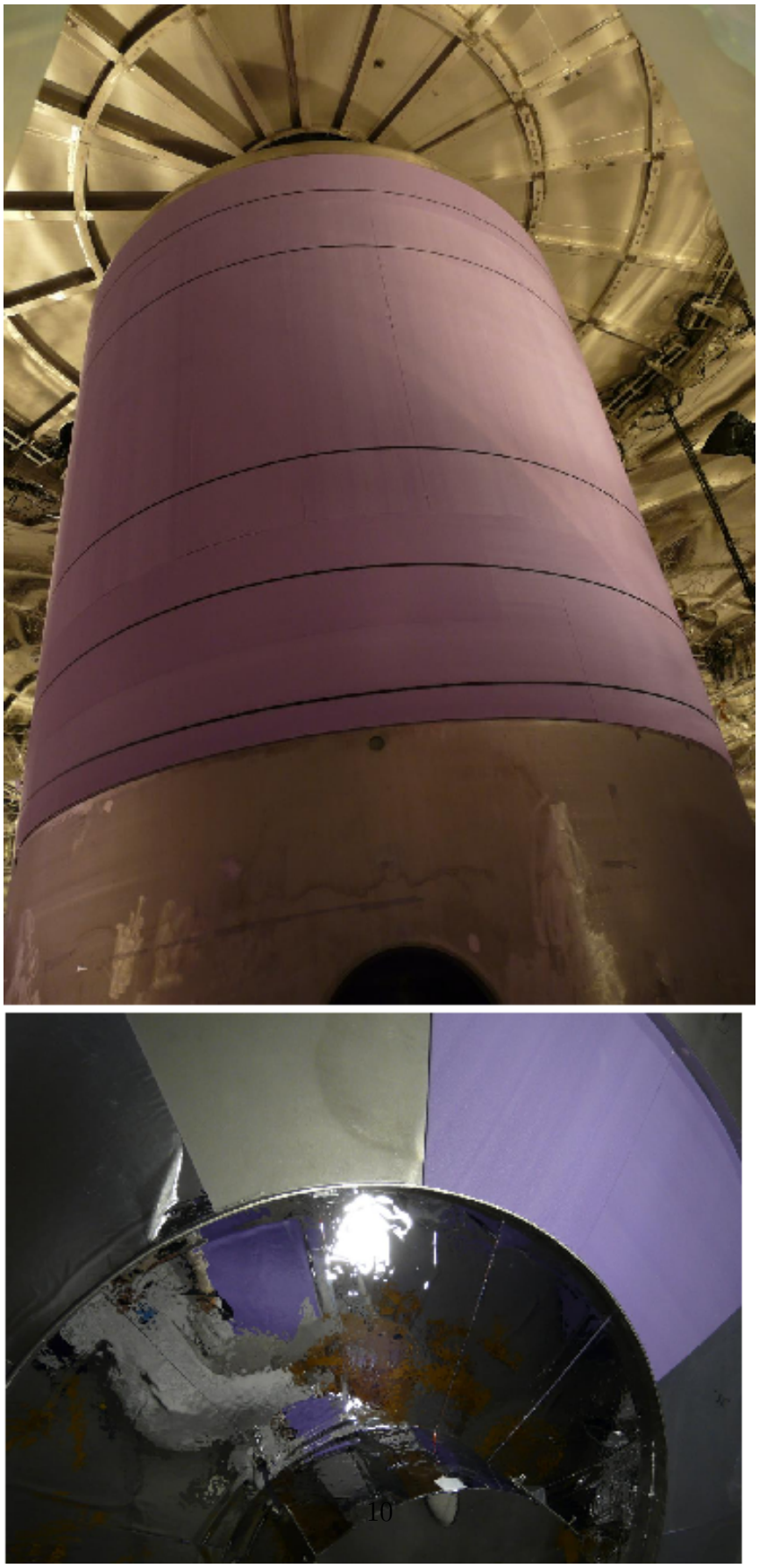

Figure 3: Jackodur mounting of the cylindrical part (top) and bottom head (bottom).

2 The Muon Veto

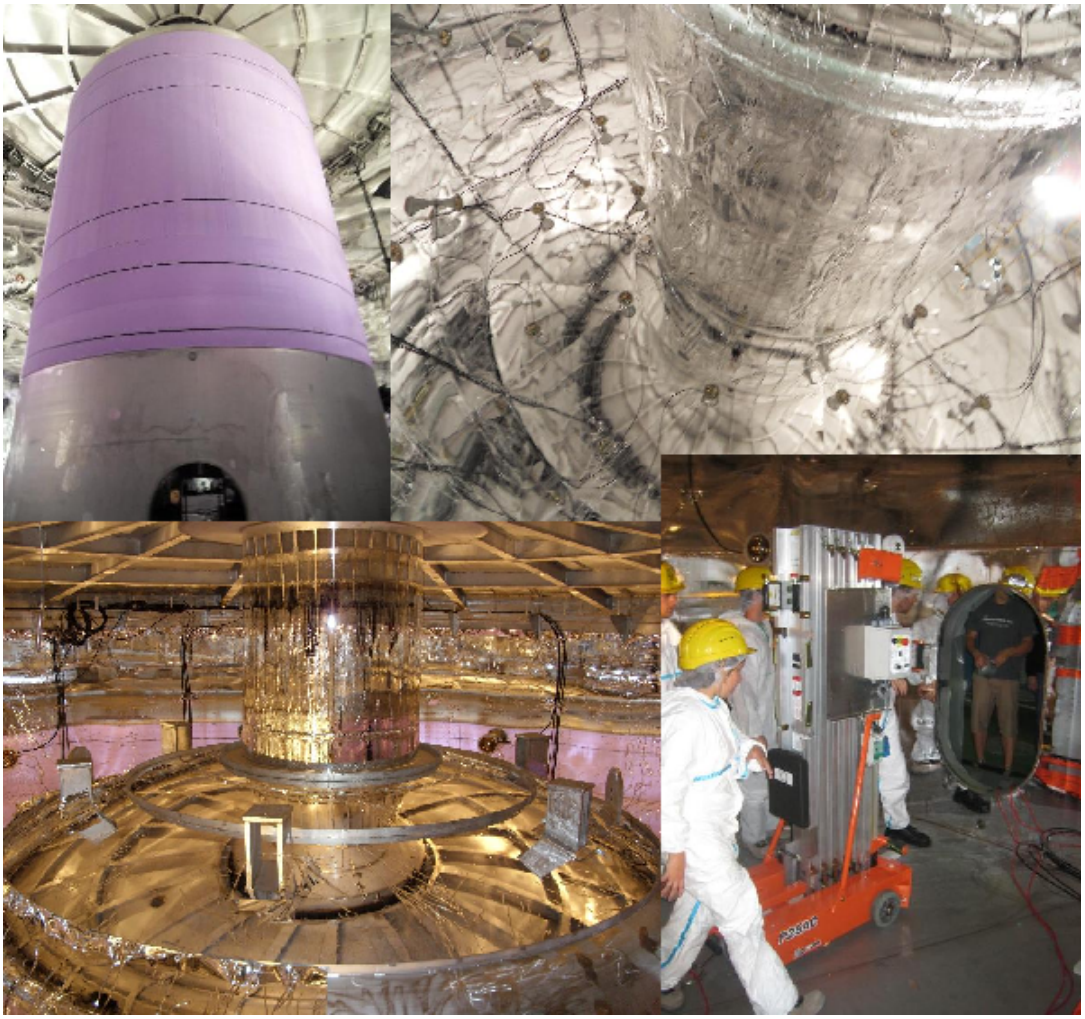

Figure 4: Collage of various impressions during mounting.

The Cerenkov Muon Veto has been installed successfully within two working periods in April and August. Already in November 2008 all the parts had been shipped to LNGS, after the tests of water proofness of the PMT capsule had been successfully completed. In April, the installation started after corrosion spots on the outer wall of the cryostat and the inner wall of the water tank the installation were removed.

The entrance into the water tank was covered on the outside by a tent of plastic foils and thus a lock was created. The water tank was declared as a clean room. The first critical point was the installation (see Figure 4) of the two personal lifters inside the water tank. The lifters were needed to reach the top of the water tank at a height of about 9 m. To fit them through the man hole they had to be dismantled in part.

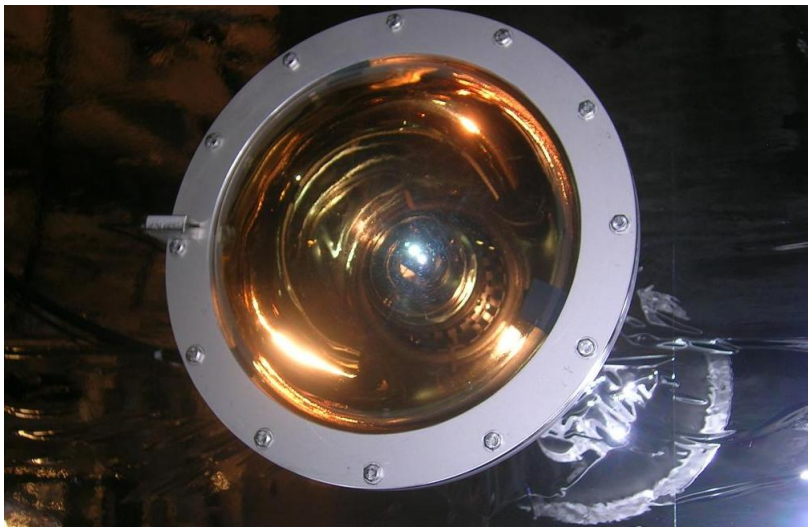

Figure 5: A photomultiplier capsule with LED light pulser in its final mounting position at the inner surface of the water tank wall.

The items to be mounted and the sequence of the procedures were:

1. install a cable tray at a height of 8.4 m at the water tank wall.
2. paste the VM2000 reflector foil on the water tank which severs also a wave length shifter for the UV Cerenkov light.
3. check the functionality of the PMTs with an LED pulser and repair in some cases.
4. mounting of the PMTs with their individual optical fibers on the wall, fixing the respective electrical cables and fibers on the wall, and feeding them through a flange in the chimney on top of the water tank.
5. wrapping of the cryostat with Jackodur for thermal insulation, mechanically secure them with plastic ribbons.
6. cover the Jackodur with VM foil glued together with a resin to achieve a water tight coverage (Figure 6).
7. insulate the bottom head of the cryostat within the pillbox with Jackodur and cover the complete interior of the pillbox with VM2000.
8. install the PMTs of the pillbox.
9. install the PMTs of the floor at an intermediate position in order to complete the works where the lifters are needed.


Figure 6: Left: Mounting Jackodur for additional thermal insulation of the cryostat as seen in the reflections in the VM2000 reflector foil of the water tank. Right: Mechanical fixation of the VM foil on the cryostat.

10. install stainless steel wires for mechanical security of the VM foil on the wall.
11. string stainless steel wires below the roof for the diffuser balls of the second LED flasher system.
12. remove the personal lifters.
13. cover the floor with VM2000 and position the relevant PMTs.
14. final check of the PMTs by LED flashers from the counting house.

The installation was accomplished in a total period of 5 weeks. The LNGS group has meanwhile installed the water distributors inside the water tank as well as some level meters. Hence all works inside the tank are finished (see Figure 7). Details about the design, the simulation and the installation can be found in the PhD thesis of Markus Knapp [1].

Thus, the water tank is ready for water filling which will be done after cooling down the cryostat and having first experience with the operation of a cold cryostat.

Work in Tübingen continued on HV slow control in collaboration with the Padova group and on data acquisition in coordination with the Heidelberg group.

For the plastic muon veto, which will be mounted on top of the clean room, a preliminary design for the mounting gear has been drafted. The procurement of a second batch of optical fibers was successful. Three km of fibers arrived in Tübingen and will be shipped to Dubna for assembly.

Figure 7: The three pictures document the stages of the muon veto installation from the empty water tank to final stage with the VM2000 reflector foils and PMTs mounted. The bottom depicts the pillbox below the cryostat showing all 6 PMT in place. The three pictures have been stichted from more than 100 individual images.

3 Phase I signal chain integration

One central activity during the last six months concerned the integration of the complete Phase I signal chain in the Hall di Montaggio of LNGS. The work was carried out in close collaboration between different task groups including TG1 (Phase I detectors), TG3 (front-end electronics), TG5 (lock system), TG8 (infrastructures) and TG9 (DAQ).

3.1 The setup in the LNGS Hall di Montaggio

An infrastructure was installed in the Hall di Montaggio to simulate the GERDA experimental setup. An 88 liter liquid argon cryostat with liquid nitrogen active cooling has been installed below an elevated platform. The glove box with the commissioning lock (Figure 8, left) is mounted on top of the platform and is enclosed by a tent which is vented with HEPA-filtered air.

Figure 8: Integration of the detector and signal chain in the Hall di Montaggio. **Left:** View of the glove box with the commissioning lock. **Center:** Mounting of the two detector string under nitrogen atmosphere. **Right:** Insertion of the detector string into the single-string arm of the commissioning lock. The liquid argon cryostat with active cooling located below the platform is not visible.

Final, or close to final components were implemented in the setup in order to identify possible interface problems. Operational procedures as e.g. the velocity to deploy the detector string in the liquid argon with the lock system or the warming up by a flow of warm and clean nitrogen gas were defined and tested. The setup was first commissioned with detector mock-ups to debug the mechanics and electronics, followed by operations with a single detector string. The final configuration consisted of a Phase I string equipped with two germanium crystals with natural isotopic composition and an additional 33 pF capacitor to simulate a third detector. The two diodes were connected with 35 cm and 50 cm unshielded copper wires to the three-channel PZ0 front-end electronics. The 33 pF

capacitor was mounted on the PCB and coupled to the third electronic channel. The PZ0 outputs were connected to the 7 m cable chain inside the commissioning lock. Figure 8 shows the mounting of the string inside the glove box under nitrogen atmosphere (center) and the insertion into the vertical arm of the commissioning lock (right). The preamplifier signals were recorded using optionally a standard spectroscopy system, a FADC readout to record long signal traces, or the Phase I FADC DAQ.

3.2 Spectroscopic performance

The spectroscopic performance of the full signal chain using a standard spectroscopic system was satisfactory. The two detector string was operated with an energy resolution of 2.9 keV (FWHM) at the 1.3 MeV ^{60}Co line (shaping time 10 μs) for both detectors, and a pulser resolution of 2.2 keV (FWHM) for a signal equivalent to 1 MeV. The pulser resolution measured with the channel coupled to the 33 pF capacitor gave a resolution of 1.2 keV (FWHM). Figure 9 displays the measured energy spectra in response to a ^{60}Co source together with the pulser. The best energy resolution so far achieved with this setup was 2.7 keV (FWHM) at 1.3 MeV.

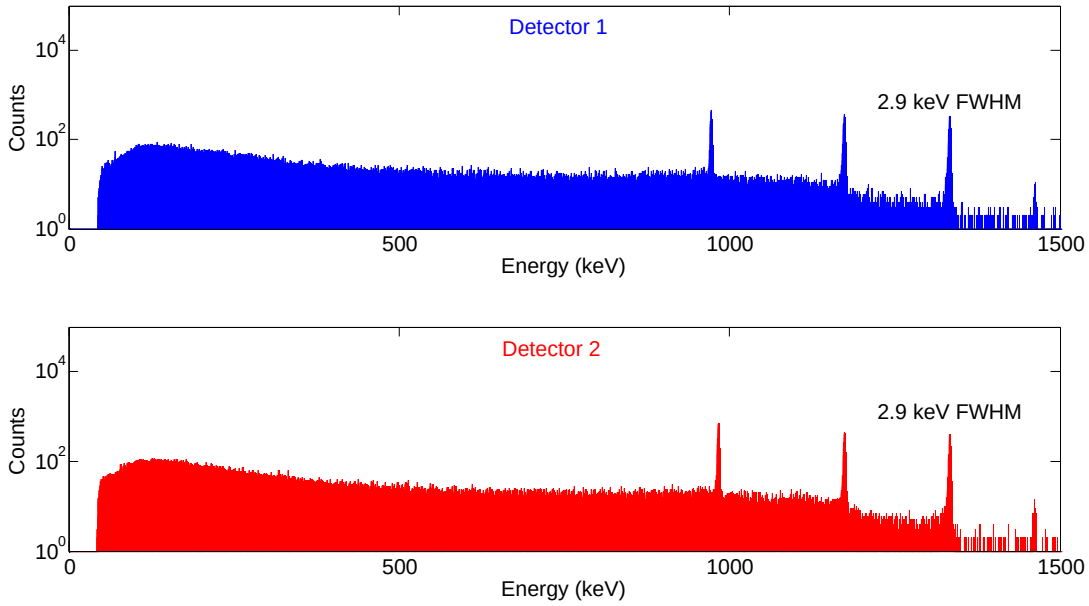

Figure 9: Energy spectrum measured with the Phase I string in the Hall di Montaggio integration test. The top spectrum corresponds to the 1.6 kg Phase I prototype detector and the bottom to the 2.3 kg GTF32 detector. The lines at 1 MeV are from the pulser.

3.3 Cross talk

A Fourier (FFT) analysis to study the noise spectra is carried out using signal traces recorded with an FADC (c.f. section 5). The analysis of the FADC data to study the optimal filtering as well as to quantify the cross talk between the channels within the above mentioned Phase I string is ongoing and preliminary results for the cross talk are available.

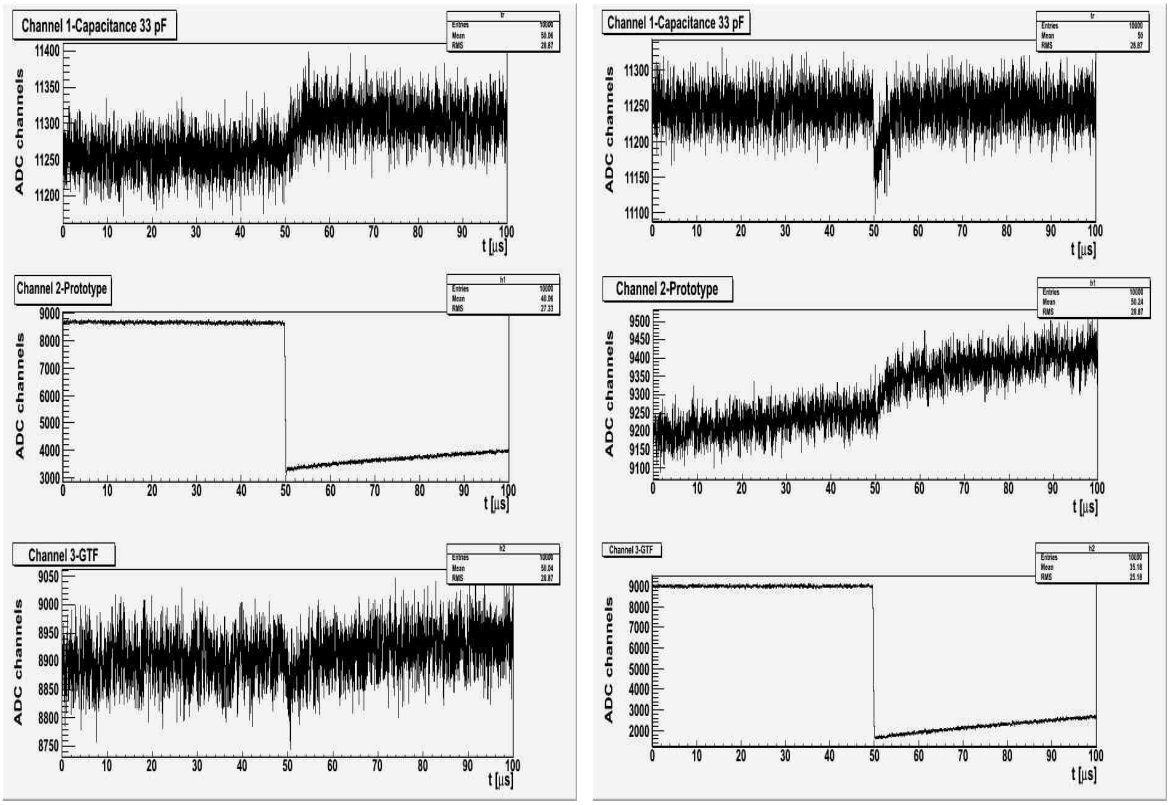

Figure 10: Pulse shapes of the Phase I detector string. PZ0 channels 1, 2, and 3 are connected to a 33 pF capacitor (top), the prototype detector (middle), and the GFT32 detector (bottom), respectively. Left: Cross talk in channels 1 and 3 for an event in the prototype diode (1.5 MeV energy deposition). Right: Cross talk in channels 1 and 2 for an event in the GTF32 detector.

A 33 pF capacitor was connected to channel 1 of the PZ0, the Phase I prototype to channel 2, and the GTF32 diode to channel 3. Figure 10 left panel shows the preamplifier signal of channel 1 and 3 when a high energy event (above 1.5 MeV) is generated in the Phase I prototype detector. Figure 10 right panel shows the preamplifier signal of channel 1 and 2 when a high energy event (above 1.5 MeV) is generated in GTF32. The pulses induced on the two not-triggered channels have different shapes and polarity, suggesting different origin of the cross talk. The induced amplitudes are 0.5% and 1% of the parent

pulse as can be seen from Figure 11, for the negative and the positive one, respectively. These values have to be compared to the cross talk measured with the encapsulated SUB detector of 1.8% and 0.8% for CH1/CH2 and Ch3/CH2, respectively. This effect needs further studies.

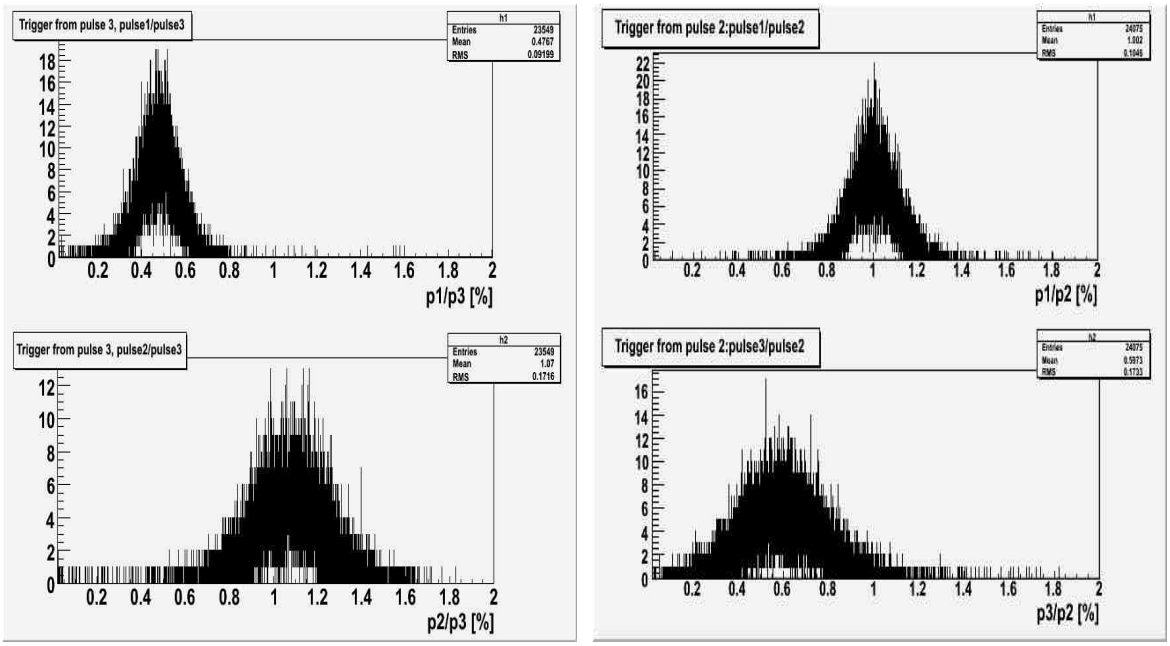

Figure 11: Distributions of the cross-talk pulse amplitudes

3.4 Integration issues

The integration was completed successfully beginning of November. It has been a major milestone to optimize the functioning and interplay of the different sub-components as well as task groups. Several interface issues and technical shortfalls could be identified. This includes mechanical modifications of the pulley system of the lock, implementation of an independent positioning measurement system of the pogo-pin matrix, as well as electrical contact problems of the pogo-pin matrix. The Phase I DAQ and on-line software is currently being debugged. Necessary modifications of the system are being implemented to ensure a smooth start-up of GERDA underground in Hall A.

4 Calibration

4.1 Monte Carlo simulations

During the last months several simulations of the Phase I detectors with the commissioning lock have been carried out, establishing the optimal number of calibration sources and their best location. In order to increase the count rates in the detectors and to maximize the signal to background ratio in the relevant peaks, the distance between the source and the detector array had to be reduced and the number of calibration sources was increased. Simulations show that two sources would not ensure sufficient and comparable statistics in all four detector strings. Therefore, the design of the cluster flange had to be changed in order to include three calibration sources placed closer to the detector strings. This required to change the size of the flanges for the calibration system from CF63 (Figure 12(a)) to CF40 in the new lock design (Figure 12(b)). The entire source lowering system will be placed between the cluster flange and glove box and the tube for the source will be bent by 90° to facilitate the access to the tubes housing the detector strings as well as those housing the sources themselves. The details of the drawings will be finalized in the next few days, with the most likely configuration being shown in Figure 12(b).

The preliminary simulations show that three ^{228}Th sources with an activity of 20 kBq/source will provide a sufficient number of events (see Table 1) for a minimum of 45 minutes of total runtime, thus confirming the results obtained with the previous detailed simulations of the final lock.

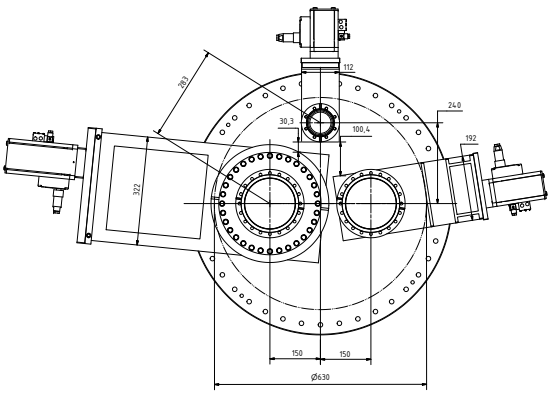

(a) **Old geometry:** the CF 63 flange for the calibration source can be seen on top.

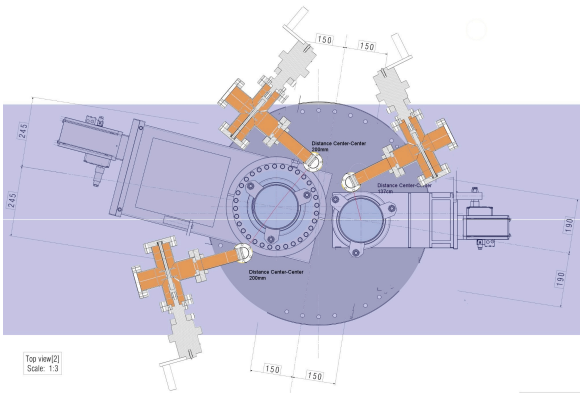

(b) **New geometry:** the three new CF 40 flanges for the calibration source are shown in orange.

Figure 12: Top view of the cluster flange including parts of the lowering system as well as the relevant dimensions. In both geometries, the CF 250 flange which will house up to three detector strings and the CF 150 flange which will house one detector string are shown on the left and right side, respectively.

^{208}Tl SEP		3 Sources	2 Sources	1 Source
A	events/h	2865 ± 54	685 ± 26	314 ± 18
	P/B	4.5 ± 0.2	3.6 ± 0.3	3.3 ± 0.4
B	events/h	1755 ± 42	818 ± 29	664 ± 26
	P/B	4.0 ± 0.2	3.2 ± 0.3	3.7 ± 0.3
C	events/h	2286 ± 48	481 ± 22	151 ± 12
	P/B	4.6 ± 0.2	2.8 ± 0.3	2.7 ± 0.4
D	events/h	2118 ± 46	524 ± 23	136 ± 12
	P/B	4.2 ± 0.2	3.4 ± 0.4	3.3 ± 0.6

Table 1: Count rates in the ^{208}Tl single escape peak (SEP) and peak-to-background ratios (P/B) for different configurations for GERDA Phase I: "3 Sources" represents the configuration shown in figure 12(b); "1 Source" represents the configuration in figure 12(a); "2 Sources" uses the same configuration as in "1 Sources", with the second source on the opposite side of the detector strings. A, B, C and D refer to the four detector strings. The provided numbers are for the top detectors of each string assuming an activity of 20 kBq per source.

4.2 Absorber

Since the size of the flange for the calibration source has been reduced in the new configuration of the cluster flange, the diameter of the absorber had to be decreased accordingly. To guarantee sufficient shielding of the photons emitted under small angles to the vertical center line, a ring made of tantalum, to be fixed below the cluster flange, has to be built. The calibration source will be parked in the Ta ring during data taking and lowered down to the detector levels during the calibrations runs. Figure 13 (left) shows the new configuration including the relevant dimensions. The first absorber and lowering system will be tested at LNGS before the next two system will be assembled. The machining of all three rings is ongoing (the first absorber has already been machined) and they will be attached the cluster flange before it is moved to Hall A.

4.3 Source Production

As reported in detail in April 2009, commercially available ^{228}Th sources are embedded in a ceramic pallet of predominantly light elements, resulting in an enhanced neutron flux from (α,n) reactions. Using SOURCES4A and the proper isotopic abundance for each material in the ceramic, a total neutron production rate of about 4×10^{-2} n/(s·kBq) (with a mean energy of 1.5 MeV) has been calculated. Simulations of the neutrons emitted in the source parking position showed that the background in the 1.5 - 2.5 MeV region is about 10^{-5} events/(kg·y·keV·kBq), which would be at the level of the GERDA phase II goal for a 100 kBq total ^{228}Th activity. A method for the production of a source with a reduced neutron flux has been investigated in collaboration with the Paul Scherrer Institut (PSI) in Switzerland. The custom ^{228}Th source is embedded in gold, suppressing (α,n) reactions due to a 9.9 MeV threshold, which is above the maximum α energy in the ^{228}Th

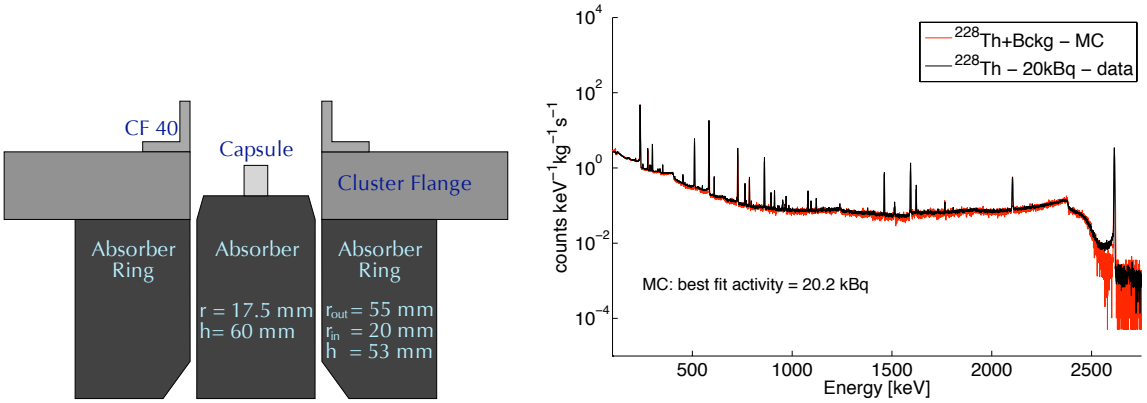

Figure 13: (Left) Side view of the tantalum ring and absorber with the source capsule in their parking position, together with an indication of the cluster flange and the CF 40 flange for the calibration system. (Right) Comparison between ^{228}Th data taken with a HPGe detector at UZH and Monte Carlo simulations. The activity of (20.2 ± 0.4) kBq was determined from a best-fit of the data to the simulated spectrum.

chain. A 20 kBq ^{228}Th-HCl solution had been processed at PSI at the end of March and shipped back to Eckert&Ziegler, Prague, for encapsulation and certification. In order to investigate the equilibrium of the ^{228}Th chain after the treatment and to measure any potential reduction in the total activity, gamma spectroscopy measurements have been carried out immediately before and after the treatment at PSI and two months later at the University of Zurich (UZH). A reduction of the ^{212}Pb peak at 238.6 keV compared to the ^{224}Ra line at 241 keV has been observed right after the treatment. This effect can be explained by a break in the chain equilibrium caused by the release of radon gas during the heating of the ^{228}Th-HCl solution. Due to the fast decay time of the ^{228}Th daughters, the restoration of the equilibrium was expected within a few weeks.

The spectrum taken with a Ge detector at UZH confirms the recovery of the chain. The measured ratio between the amplitude of the ^{212}Pb and the ^{224}Ra peak of 10.4 ± 0.3 is in good agreement with the expected value of 10.6. In order to estimate the total activity of the source after the treatment, a full Monte Carlo simulation of the HPGe detector at UZH has been carried out in the framework of GEANT4. In Figure 13 (right) the simulated spectrum (red) between 50 keV–2.7 MeV is compared with the real data (black). The activity has been estimated in a χ^2-minimization of the fit of the data to the MC spectrum. The obtained value for the activity is (20.2 ± 0.4) kBq, thus showing no significant losses.

To detect any leakage in the stainless steel capsule of the source, a wipe test has been carried out. Two different wipes have been collected: in the first, the sealed capsule was wiped with ethanol (WIPE-I), in the second, the sealed capsule was folded into filter paper and immersed in liquid nitrogen for a few minutes (WIPE-II).

The wipe samples have been then shipped to LNGS where they were screened with an ultra-low background HPGe spectrometer (Gator) for about 1.8 days each. Figure 14 (left)

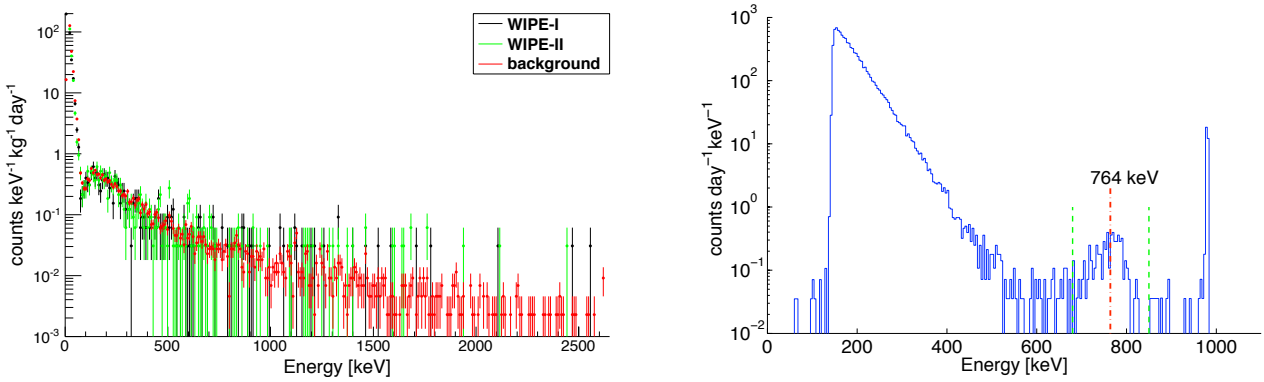

Figure 14: (Left) Energy spectra from WIPE-I, WIPE-II and background measured with the GATOR HPGe detector at Gran Sasso underground Laboratory. (Right) Measurement of the neutron rate emitted by a 20 kBq custom ThO_2 source with a ^{3}He counter operated underground at LNGS. The neutrons are detected via the ^{3}He(n,p)^{3}H reaction with a Q-value of 764 keV. The continuum is due to wall effects (for interactions which happen close to the detector walls some of the energy of the protons gets lost) in the ^{3}He tube and is accounted for in the calculation of the detection efficiency.

shows the spectra of the two wipes (black, green), compared with the background of the detector (red). For both samples, no counts above the background were observed within the collected statistics. The derived upper limits using three gamma peaks from the ^{228}Th chain are at the level of a few mBq and are given in Table 2.

Sample	^{208}Tl (583 keV) [mBq]	^{208}Tl (2615 keV) [mBq]	^{212}Pb (238.6 keV) [mBq]
WIPE-I	< 1.2	< 5.3	< 1.8
WIPE-II	< 1.1	< 5.1	< 1.7

Table 2: Upper limits in ^{228}Th contamination resulting from the wipe tests performed on the sealed source capsule.

The neutron rate of the custom ^{228}Th source had been predicted to be about two orders of magnitude lower than the one of a standard source (the residual neutrons coming from reaction on ^{17}O and ^{18}O, which are present at the level of 0.04% and 0.2% in the natural oxygen of the ThO_2 source). This neutron rate has been measured with a ^{3}He counter at LNGS. To moderate the high energy neutrons produced in (α,n) reactions down to thermal energies, 12.5 cm of polyethylene around the ^{3}He counter have been used. After $\approx$ 28 days of live time, the observed neutron rate was (0.017 $\pm$ 0.003) n/s, in relatively good agreement with the predicted value of 0.01 n/s. The unknown contaminations of Zr and Fe in the ^{228}Th solution, which have not been considered in the calculations of the neutron flux, could explain the difference between the measured and the calculated rates.

The spectrum taken with the ^{3}He counter and the region of interest around the Q-value of 764 keV are shown in Figure 14 (right).

To further confirm the n-flux reduction, neutron measurements with a commercial ^{228}Th source are planned. To ensure a total of three 20 kBq ^{228}Th sources for GERDA Phase I, two additional customized sources will be prepared at PSI before February 2010 (the order for the ^{228}Th-HCl solution has been placed).

5 Status of Front End Electronics

5.1 FE circuits test in HdM commissioning setup

One 3-channel charge sensitive amplifier (CSA) based on the PZ0 ASIC (1.4 pF compensation in the ampfifying node) with discrete JFETs at the inputs was used in the HdM commissioning setup (see Figure **??**). The circuit is mounted inside a copper shield to protect against electromagnetic (EM) pickup noise and fixed at the copper frame which holds the detectors, as shown in Figure 16. The distance to the detector is determined by the radioactivity of the circuit. It is about 35 cm. Unshielded cables are used to connect the detectors to the CSA inputs. This circuit has been used since July until now. It underwent many thermal cycles which shows its reliability.

A bundle of 10 PTFE sub-miniature coaxial cables (C = 94 pF/m, R = 1 Ω/m) passes from the feedthrough flange of the commissiong lock through a cable chain to a Pogo pin matix which provides the mechanical support and the electrical connection of the assembled string. The 10 cables are for the CSA outputs (3), the test pulse (1) and low voltage power (6). For each of the two supply voltages, 3 cables have been combined to reduce the resistance down to $\approx$3 Ω, and thus to minimize the effect of the voltage drop when the circuit draws current to drive the output signals. In addition, there are 4 PTFE miniature coaxial cables for high voltage.

Durning the tests, several spring contacts of the Pogo pin matrix failed as a consequence of thermal cycles. Consequently, it was decided to bypass the matrix and to use regular flat band connectors.

The scheme followed in the tests is the following

- **Test with capacitors**: Exploiting the 3 channels of the CSA and connecting 33 pF capacitors at the inputs to simulate the detectors, it has been possible to optimize the grounding configuration of the setup, to minimize environmental EM pickup, to check the noise introduced by the active cooling or the boil-off of the LAr bath, and to improve the energy resolution. The 3 capacitors are connected differently to the inputs:
  - channel 1: SMD capacitor on board. This allows to evaluate the adopted grounding scheme and the electrical connections.
  - channel 2: disk ceramic capacitor located just outside the copper shield connected to the circuit with *short leg* (SL). It is used to evaluate EM pickup in the environment (dewar, lock, etc) where the detector will be located.
  - channel 3: as channel 2 but the cables connecting the capacitor to the circuit are as long as for the detector connection (*long leg*(LL)). It allows to evaluate i) microphonic noise, ii) EM pickup with the real cable length, and iii) effect of the high voltage connection.
- **Test with detector(s)** applying the best contacting, grounding, and shielding configuration obtained in the tests with capacitors.

In Figure 16 the two capacitors external to the copper shield are visible.

The results obtained with capacitors and with the prototype detector connected are summarized in Figure 17.

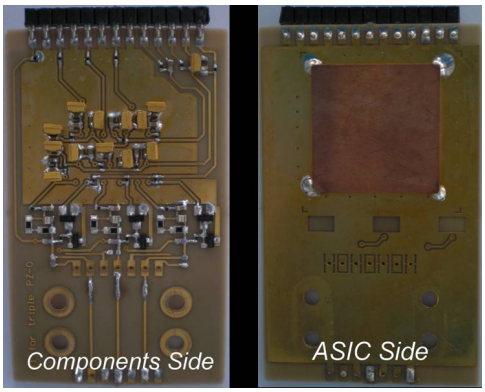

Figure 15: The 3-channel CSA based on the PZ0 ASIC. Left: component side. Right: ASIC side. The ASIC is shielded by a copper housing.

The energy resolution achieved so far for the naked prototype detector coupled by a 35 cm long unshielded wire to the CSA is 2.9 keV @ 1332.5 keV ^{60}Co line. The pulser line width is 2.3 keV, to be compared to 2 keV when the detector is replaced by a 33 pF capacitor and a dummy to reproduce similar mechanical vibration frequencies. In the latter case the cable length was identical and high voltage was applied. In previous tests, coupling the same CSA to the SUB encapsulated detector, an energy resolution of 2.6 keV was achieved at the 1332.5 keV ^{60}Co line.
Therefore an extra noise source of $\sim$1.3 keV is present, when the circuit is connected to the naked detector in LAr. This extra noise cannot be attributed to the leakage current of the detector which was always around 10 pA. Besides the observed microphonic contribution, the noise frequency analysis of baselines waveforms indicate a 1/f component (see Figure 18). The latter could arise at the interface between the naked detector and the LAr (where the bias voltage drops). Noise frequency analysis and spectroscopic measurements are consistent.
In the run with two detectors connected (prototype and GTF32) it has been possible to achieve 2.9 keV resolution at the 1332.5 keV ^{60}Co line on both detectors but much more low frequency noise showed up. This is clearly shown in the comparative noise frequency analysis in Figure 18.

5.2 Radioactivity of the circuit

The first γ-ray activity measurements of the assembled PCB indicated an acceptable ($\sim$ 200 μBq/PCB) ^{228}Th concentration but an extremely high ^{226}Ra (6.3 mBq/PCB) concentration. These values have to be compared to the allowed limits of 500 μBq/PCB for

Figure 16: The circuit is mounted inside a copper EM shield and fixed at the frame that keeps the detectors string. The two capacitors (*short leg* and *long leg*) are visible. The cables connecting the detector (or capacitors) to the circuit are fixed to minimize vibrations. The HV lines are visible at the left side of the circuit box.

Working Temperature	89 K		
Rise Time		SM 50 + RG 174	SM 50
	Ch-1 (C_{DET}=33 pF, on board)	74 ns	40 ns
	Ch-2 (C_{DET}=33 pF, short leg ~1 cm)	72 ns	41 ns
	Ch_3 (DETECTOR)	73 ns	41 ns
Fall Time	250 µs (R_F = 1 GΩ, C_F = 0.3 pF)		
Resolution	Ch-1 (C_{DET}=33 pF, on board)	1.2 keV @ 1 MeV pulser line	
	Ch-2 (C_{DET}=33 pF, short leg ~1 cm)	1.2 keV @ 1 MeV pulser line	
	Ch-3 (DETECTOR)	2.9 keV @ 1.332 MeV (60Co) 2.3 keV @ 1 MeV pulser line	
Power Required (T=77K)	~ 40 mW (V_{FET} = +3.7 V, I_D = 3 mA; V_{CC}= +3.1 V; V_{EE} = -2 V)		

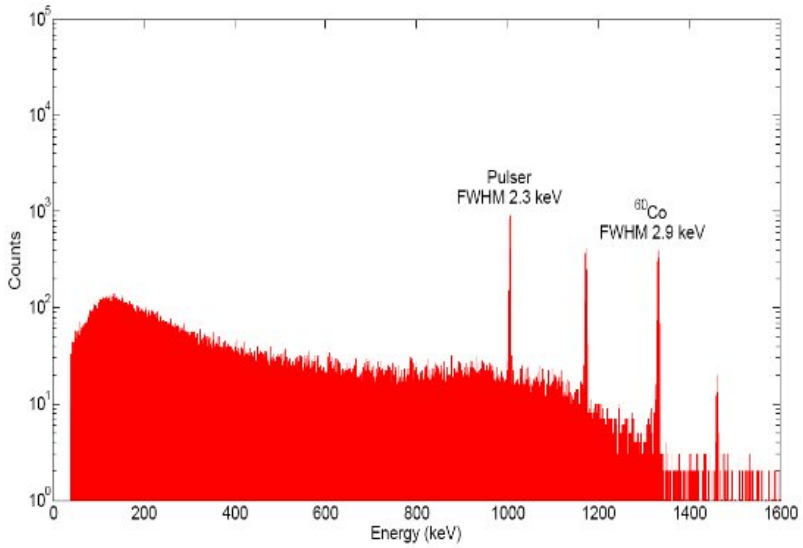

Figure 17: Top: FWHM and pulse rise time values achieved on the 3 chs with capacitors and with prototype naked detector. Bottom: the recorded ^{60}Co spectrum.

^{228}Th and 2.5 mBq/PCB for ^{226}Ra to keep the background index in the DBD window $< 10^{-3}$ cts/(keV·kg·y). In subsequent measurements the cause of the ^{226}Ra contamination has been found in the ceramic capacitors of type X5R, X7R, and to a minor extent of NP0 type. After substituting all the X5R and X7R capacitors with Tantalum ones, the PCB has been re-measured (still ongoing): the results are satisfactory i.e. a factor 10 reduction of ^{226}Ra while the ^{228}Th can not be determined (<400 μBq) with the present available statistics. The residual ^{226}Ra content is fully due to the NP0 capacitors.

5.3 PZ0: Next steps

The PZ0 output stage has been redesigned to drive 50 Ω load at cryogenic temperatures, and improve the cross talk among channels related to the low voltage power supply. The

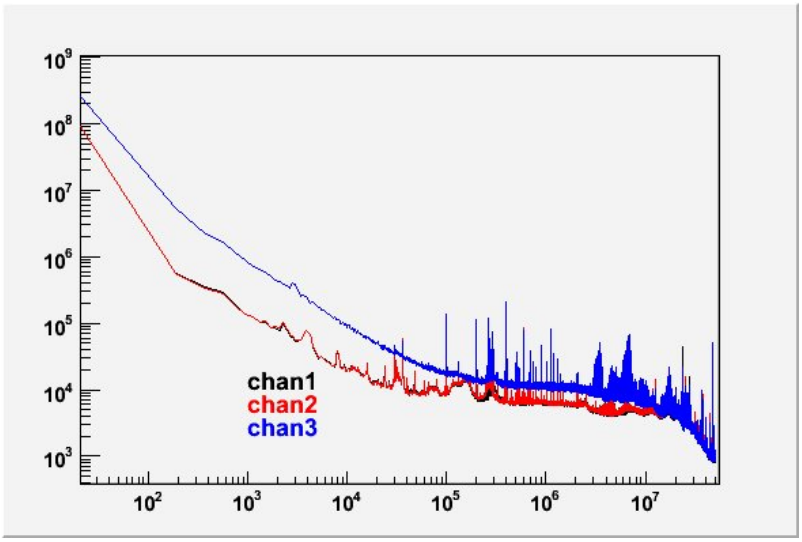

Figure 18: The noise frequency spectrum built up from baselines waveforms for the two channels (red and black) with the capacitors and for the channel with the detector (blue). The noise spectrum of the detector in the relevant frequency range has a 1/f trend.

production at the foundry is ongoing and delivery is expected by the end of the year.

5.4 Test of a CSA based on commercial CMOS OPAMP

In the last semester, the CSA circuit shown in Figure 19 based on a commercial CMOS OPAMP (CC2) of the family OPA35x has been tested at the bench, with the encapsulated SUB detector, and with a capacitor at the input in the HdM setup. The OPAMP is operated in a closed loop configuration as the second stage after an external JFET (Philips BF862).

In the test with the encapsulated detector, the achieved energy resolution was 2.6 keV at the 1332.5 keV ^{60}Co line, as good as for the CSA based on the PZ0. But at cryogenic temperatures, the pulse rise time is poorer than for the PZ0 and, moreover, is limited in slew rate. A few more OPAMPs will soon be tested at cryogenic temperatures to verify their slew rate. The slew rate problem can be corrected by putting two stages in cascade. A CSA based on commercial CMOS OPAMP has the advantage of easiness and, compared to the PZ0 ASIC in the current version, reduces the number of discrete components on board by about 50%. This has the evident advantage for the radiopurity issue.

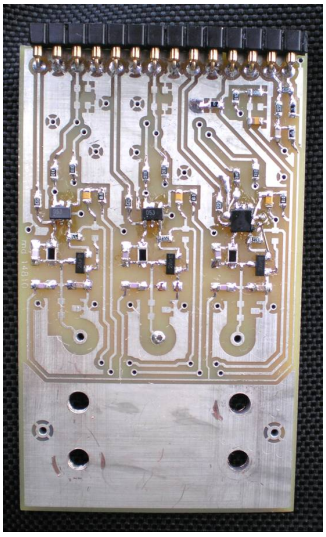

Figure 19: The CSA based on Commercial CMOS Amplifiers.

6 Phase I detectors

The activities of task group one (TG-1) focused on the Phase I signal integration test carried out in the Hall di Montaggio of the LNGS, as described in Sec. 3, and on the commissioning of the low-background test stand LARGE in the underground Germanium Detector Laboratory (GDL).

6.1 Low-background test stand LARGE

Following the successful test commissioning of the LARGE cryostat, its active cooling system, and the PMTs in Heidelberg, the cryostat and all components were dismounted, cleaned by degreasing, and etching, packed and shipped to the LNGS underground laboratory. The cryostat was then mounted in its shield in GDL. Subsequently, the assemblies internal to the cryostat which include the wavelength shifting reflector foil, the PMT bank, the temperature sensors, the optical fibers, and the calibration tube were installed. After closing the cryostat top-flange, all external connections as cryogenic supply and cooling lines, auxiliary tubing, cables for the PMT signal, for the high voltage supply, and for the temperature probes, were mounted and fed through the shield. Figure 20 shows various stages of the mounting.

Figure 20: Integration of the low-background test stand LARGE in GDL. **Left:** View of the PMT bank prior to installation inside the cryostat. **Center:** View from the inside of the cryostat on the PMT bank and the reflecting wavelength shifting foil covering the internal walls of the cryostat. **Right:** View on the top flange of the cryostat with the vacuum insulated cryogenic lines and signal feed throughs.

Residual volatile impurities inside of the cryostat were removed by flushing with argon gas and by repeated pumping and pressurizing of the cryostat. The gaseous impurities were measured with a mass spectrometer. During argon gas flushing, the concentration of nitrogen, oxygen and water were below the sensitivity of the mass spectrometer which was approximately 10 ppm. After insulating the cryostat, the nitrogen and oxygen concentrations increased by about a factor of ten at room temperature and a factor of three when the

cryostat was cooled to -150 degrees prior to filling. In addition the gas quality was monitored by the pulse height and triplet life time of the scintillation light created by an alpha source which was lowered along the symmetry axis of the cylindrical cryostat. Figure 21 shows the mean pulse shape of the scintillation light of the alpha source in the argon gas phase. The measured life time of the slow component (triplet state) $\tau = 2.50 \pm 0.05$ μsec.

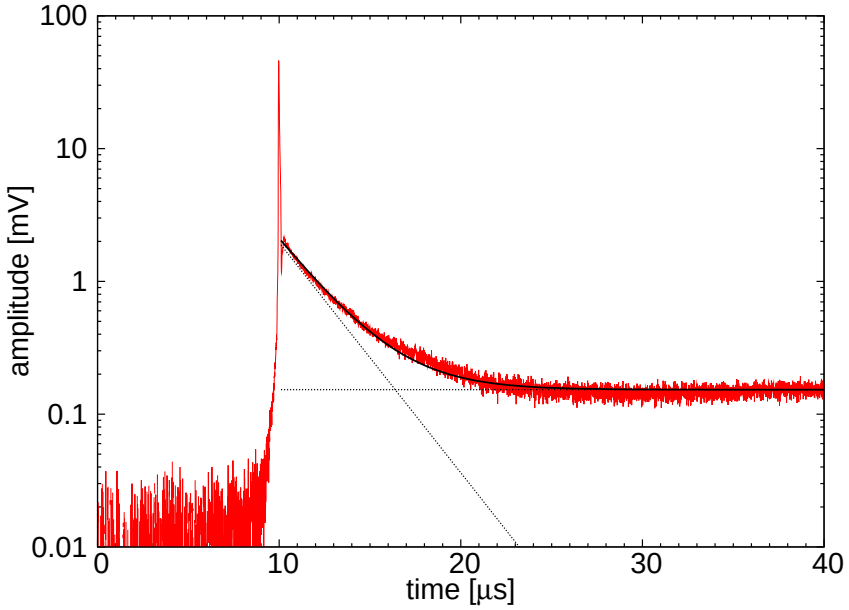

Figure 21: Mean pulse shape of the scintillation light of argon gas at atmospheric pressure in response to alpha radiation from the Gd-source. The life time to the slow component is $\tau = 2.50 \pm 0.05$ μsec.

The pre-cooling of the cryostat started October 29 and the liquid argon filling was carried out on October 31 and November 1. The liquid argon passed through a low-temperature charcoal trap to remove residual radon and was filtered afterwards.

The liquid argon is sub-cooled to -188 ^{o}C (boiling temperature is -186 ^{o}C) with a liquid nitrogen flow corresponding to 2.2 m^3/hour (STP). The gas blanket of the cryostat is insulated and the active cooling is controlled by adjusting the nitrogen flow such that the argon gas pressure is kept at about 960 mbar (absolute). The cryostat is therefore operated with $\approx$50 mbar overpressure with respect to the ambient pressure to avoid radon contamination from the air through e.g. the pressure relief valve. The filling height is stable and no argon is lost in this operational mode. The next steps are the start-up of the PMTs, their calibration, monitoring of the scintillation light yield and first background measurements of ^{39}Ar and of radon.

7 Phase II detectors

7.1 Test of 18-fold segmented n-type prototype

Last year an N-type 18-fold segmented HPGe detector was operated in a test stand in Munich for five months in liquid nitrogen. The test showed that operating N-type segmented HPGe detectors directly in a cryoliquid is a feasible solution for Phase II of the experiment.

The cryoliquid used in the GERDA experiment is liquid argon. To test the stability of the N-type HPGe detector in liquid argon, another long term test was done using one of the prototypes. No data was taken, only the leakage current was monitored continuously. It was found that the leakage current of the crystal did not change considerably during the test.

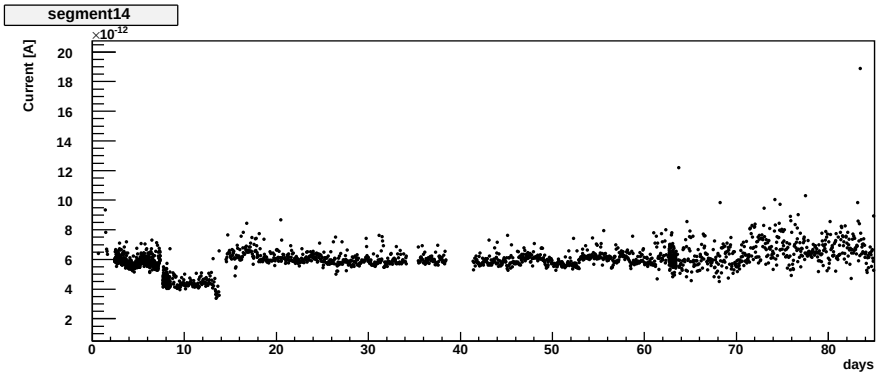

Figure 22: Leakage current of one segment of the prototype detector monitored for 90 days, measured every hour.

7.2 Production test for thick-window p-type BEGe detectors

The full production chain test for thick-window BEGe detectors starting from depleted germanium material continued during the last six months. The objectives of these efforts are to 1) investigate whether thick-window BEGe detectors can be produced based on the material supply and processing chain as envisioned for the enriched germanium material, and 2) to investigate how many kg of detectors can be produced in the future starting from 37.5 kg of enriched germanium. The depleted germanium is coming from the same supplier in Russia (ECP) and undergoes the identical chemical treatment. It is therefore the best proxy material to test the production and processing chain.

Table 3 gives the milestones achieved so far. The measured net-impurity concentration of the crystals is as low as $1 \cdot 10^{10}$ cm^{-3}, qualifying the starting material and the production chain to be suitable for BEGe detector production. After completion of the fourth crystal pulling, which is currently planned for November 11, germanium slices (detector blanks) will be cut and four to five of them will be selected for detector production at Canberra,

Olen, Belgium. The detectors mounted in standard cryostats will become available for characterization early in 2010.

28.01.2009:	Order of 34 kg depleted GeO_2 at ECP, Russia
30.04.2009:	Delivery of depleted GeO_2
05.05.2009:	Quality control of GeO_2 by ICPMS at LNGS
12.05.2009:	Start of chemical reduction and zone refinement at PPM, Germany
22.06.2009:	21.4 kg of Ge bars (6N) delivered to GERDA
08.07.2009:	Ge bars arrived at Canberra, Oak Ridge, US
17.07.2009:	Zone-refinement completed and bars cut into slices
04.08.2009:	First crystal pulled
28.10.2009:	Three crystals available with impurity conc. within specifications

Table 3: Achieved milestones of full production chain test with depleted germanium for the BEGe prototype production.

7.3 Reduction and zone-refinement of enriched germanium material

During previous purification tests with depleted germanium, PPM Pure Metals showed that they can produce material that is clean enough to start crystal pulling without additional cleaning procedures. The contamination levels were measured with mass spectrometers and the material was found to correspond to the specifications. Crystal pulling tests at IKZ and at Canberra (US) confirmed that the material from PPM does not contain contaminants that would exclude its use for High-Purity germanium production.

After the quality of the PPM material was confirmed, we decided to proceed with the purification of the enriched material. The contract is under preparation and the terms of the contract were already agreed on with PPM.

The purification of the 37.5 kg of enriched germanium will take place during the following months, possibly at the beginning of next year.

During crystal pulling tests at IKZ it was realized that the source of impurities is the Czochralski puller itself. Each and every crystal showed high levels of As, making it impossible to achieve the purity required for HPGe detectors. The best results obtained showed an impurity concentration between $10^{11}/cm^3$ and $10^{12}/cm^3$, one to two orders of magnitude higher than the level necessary for the production of HPGe detectors. It was decided to clean the puller by means of electro-polishing. The procedure required that the puller was taken apart. It was transported to an external company for electro-polishing. It is expected that the puller will be operational again at the end of October and some test crystals will be produced still this year.

7.4 Crystal characterization

Until now, IKZ grew 15 Czochralski crystals in total. Crystal characterization is performed at IKZ (low temperature Hall-effect measurements and Photo Thermal Ionization Spectroscopy (PTIS)) and at the TU Dresden (Photoluminescence (PL) spectroscopy). With both techniques the main donor impurities, namely arsenic and phosphorus, can be detected (see Figure 23).

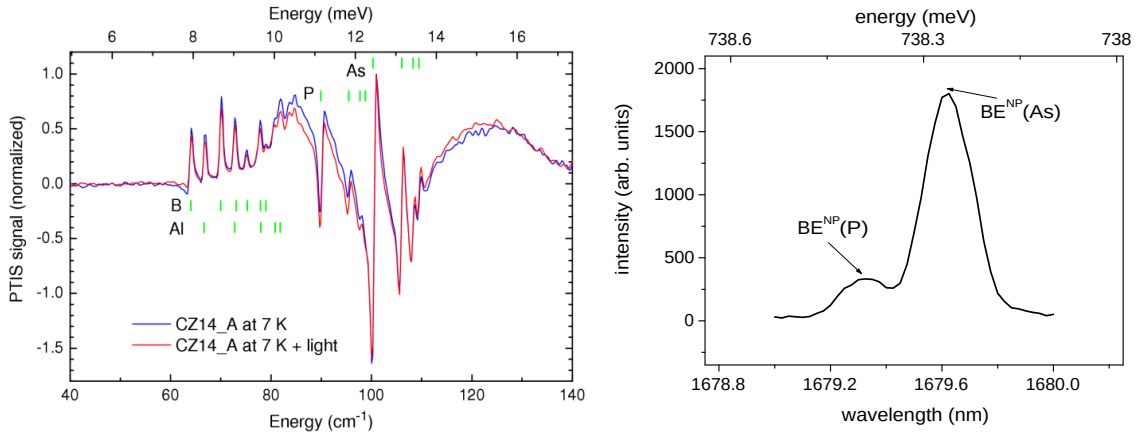

Figure 23: Comparison of PTIS (left) and PL (right) spectra of the same crystal (Cz#14)

8 Clean Room and the Lock Systems

8.1 Clean Room

The Clean Room installation is finished. It is operational since May 2009 and the approval was successful. The required clean room class was achieved within the whole room volume within 15 minutes after switching on the ventilation system. A long term test of the air conditioning verified that even under harsh conditions when the clean room was partly opened to the tunnel surrounding, the temperature and humidity were stable within the requested range. The gas- and vacuum systems will be installed during the last quarter of 2009.

8.2 The Commissioning Lock system

A temporary commissioning lock system has been installed in the Hall di Montaggio for mechanical and front end electronics tests (see section 3 for details). In the course of the work with this system, some critical handling issues could be identified. These have led to design modifications that are presently being implemented to the second cable arm at the Max-Planck-Institut für Physik in Munich. Finishing of the arm of the improved commissioning lock system is scheduled for the end of the year 2009. Installation of the

Figure 24: GERDA clean room on top of the cryostat.

commissioning lock system on the GERDA cryostat is scheduled for the first quarter of 2010. A second cable arm capable of housing up to three strings of detectors will be implemented in 2010. This will ensure that all available enriched detectors can be placed within the cryostat in hall A.

8.3 Final lock system

The design of the final lock system for deployment of up to 16 detector strings has been finalized. Due to the findings in the commissioning lock system some modifications have to be done. The lock cylinders and arms have been ordered. Delivery is expected in February 2010. Installation of the system will start as soon as work on the commissioning lock has been finished.

9 Simulations and background studies

9.1 Simulations of BEGe detectors

During the last six months a substantial amount of activity was devoted to the characterization and study of Broad Energy Germanium (BEGe) detectors [2], operated in Heidelberg, LNGS, Zurich, and Hades. The experimental activity has been complemented by Monte Carlo simulations, that have also been used to help with the data interpretation. Furthermore, progresses have been achieved in the development of a full-chain simulation able to produce realistic electronic pulses from a BEGe detector.
In particular, the BEGe test stands available at LNGS and in Heidelberg have been simulated using the GEANT4-based MAGE application. The MAGE simulation has a double

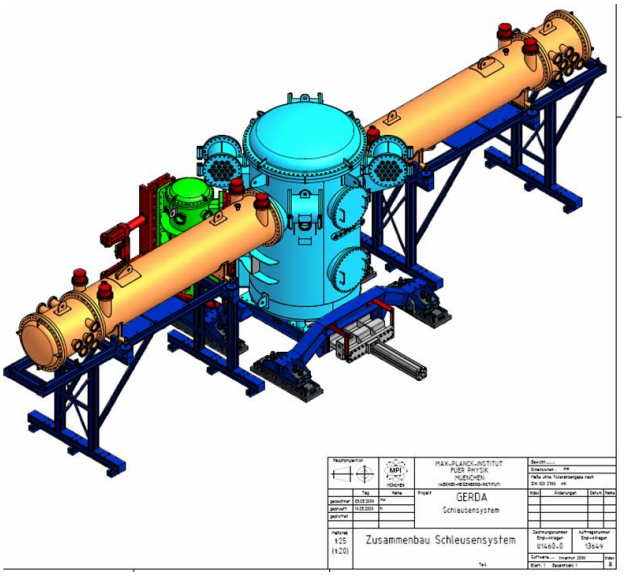

Figure 25: Drawing of the final lock system. The cylinders of inner and outer lock (blue and green, respectively) and cable arms (orange) are in production

.

aim: (1) to simulate the expected energy spectrum in the detector when irradiated with radioactive sources (^{133}Ba, ^{60}Co, ^{228}Th); (2) to estimate the pattern of the individual energy deposits within the crystal active volume. Energy, position and time of the individual energy deposits can be then be fed as inputs to a dedicated code in order to produce realistic electronic pulses (see Sect. 9.1.2) taking into account the distance among the sites where charge is released.

9.1.1 Dead layer and event topology

The dead layer of the BEGe detector available at LNGS (71 mm diameter, 32 mm height, from Canberra) has been evaluated using the same procedure [3] followed for the BEGe detector available in Heidelberg (81 mm diameter, 32 mm height). The detector was irradiated with a ^{133}Ba source and the ratio R between the intensities of the full-energy γ peaks at 81 keV and 356 keV was measured. The value of R depends on the thickness of the dead layer, which affects in a different way the two γ-rays: Monte Carlo simulations based on MaGe were run to predict the dependency of R on the dead layer thickness. Figure 26 displays the value of R derived by the simulation versus the thickness of the dead layer; the dependency has been modeled by a quadratic function (red line). The blue band represents the experimental value (with 1σ uncertainty). The resulting top dead layer thickness is hence $d = 0.79 \pm 0.03 \pm 0.09$ mm, well consistent with the Canberra specifications (0.8 mm). The lateral dead layer has been evaluated in a similar way, although with a much larger systematic uncertainty due to the fact that the detector is surrounded by a

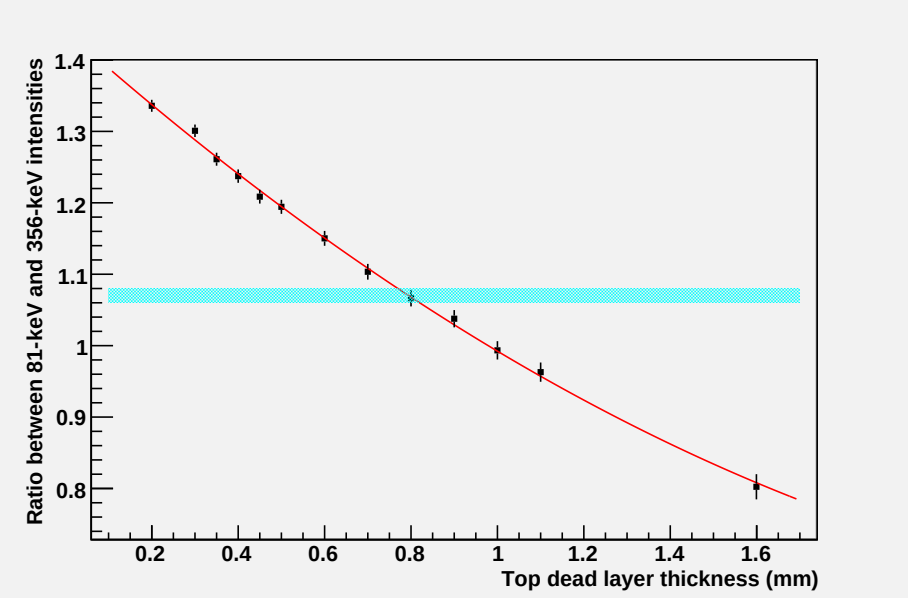

Figure 26: Monte Carlo simulation of the ratio R between the intensity of the 81-keV and 356-keV γ lines from ^{133}Ba detected by the LNGS BEGe detector, with different assumptions on the thickness of the dead layer in the top window. The Monte Carlo values have been fitted with a 2^{nd}-degree polynomial (red solid line). The light blue area is the measured value of R with 1σ uncertainty.

Cu holder, which absorbs γ-rays and whose thickness is not precisely known.
Figure 27 shows the experimental spectrum from the ^{133}Ba source (placed above the top window of the detector) superimposed with the absolutely normalized Monte Carlo simulation (added to the background). The qualitative agreement is in general satisfactory, when one takes into account the uncertainty on the source activity.

The same Monte Carlo simulation has been also used to estimate the ratio of single site events (SSE) to multi-site events (MSE). It has been shown in Ref. [4] that a suitable parameter to be used for this purpose is R_{90}, namely the radius of the sphere containing 90% of the total energy deposit. Figure 28 shows the distribution of $\log_{10} R_{90}$ for ^{208}Tl decays occuring in front of the top window of the LNGS BEGe detector. The two main structures are interpreted as due to single-site events (e.g. electrons), whose energy is released within a few hundred μm, and to multi-site events (e.g. multi Compton scattering of γ-rays), releasing energy in a radius > 1 cm. The red curve in Figure 28 is the $\log_{10} R_{90}$ distribution for the events in the double escape peak (DEP) of the 2614 keV γ-line at 1592 keV. As expected, the DEP sample is highly enriched in single-site events, with a minor contamination from MSE due to the Compton continuum.

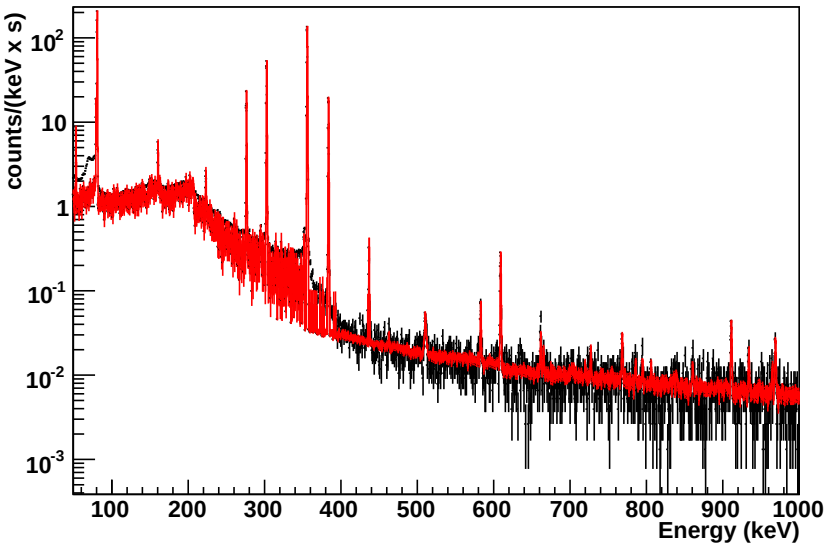

Figure 27: Energy spectrum from the LNGS BEGe detector irradiated with a 105 kBq ^{133}Ba source placed above the top window (black histogram). The superimposed red histogram is the sum of the absolutely normalized Monte Carlo simulation (based on MaGe) and the experimental background.

9.1.2 Simulation of pulse shapes

To study the performances and the features of BEGe detectors, a complete simulation of the pulse signal formation and evolution was developed. This was the first time a BEGe detector was completely simulated considering all the underlying physical processes occurring in a semiconductor detector.
The implementation of the simulation is divided into three steps. The first part is the transport of electron and γ-rays in the detector using the MaGe framework, as described in Sect. 9.1.1. In the second step of the process, the information from the MaGe simulation (energy, position and time of individual energy deposits in the detector) is taken into account to calculate the collection trajectories of the charged carriers according to the mobility models of Refs. [5, 6]. Since these models provide the charged carrier drift velocity as a function of the electric field, also the electric potential inside the crystal was calculated. Figure 29 shows the electric potential computed for the BEGe detector installed at LNGS. After the trajectories are computed, the signals induced on the electrodes by the movement of the charged carriers are calculated with the Shockley-Ramo theorem. This second part of the simulation is performed through a software based on the MGS code [7]. The last simulation step takes into account the response of the electronic chain. Pulses are convolved with the preamplifier transfer function which was experimentally determined through devoted measurements carried out with a high-precision pulser.

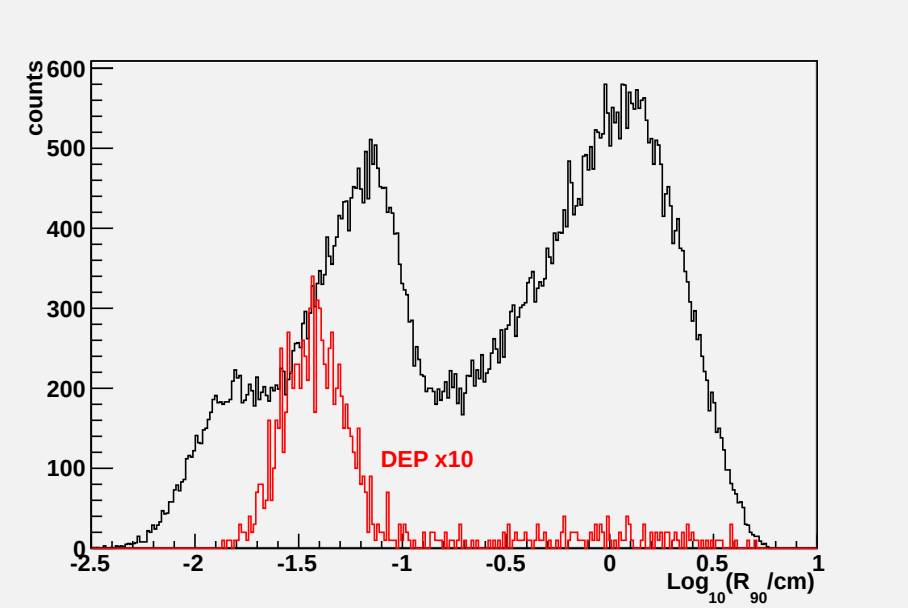

Figure 28: Distribution of $\log_{10} R_{90}$ derived from the Monte Carlo simulation of the LNGS BEGe detector irradiated with ^{208}Tl. R_{90} is defined as the radius of the sphere containing 90% of the total energy deposited in the detector and it is calculated according to the procedure described in Ref. [4]. The black histograms is the distribution for all events above 500 keV, while the red one is restricted to the 1592 keV events from the double-escape of the 2614 keV γ-ray.

To validate the simulation, a set of specific measurements was carried out. The pulse shapes of experimental and simulated signals for different interaction positions were directly compared. The LNGS BEGe detector was irradiated with a collimated ^{241}Am radioactive source in different positions; the source emits low-energy 59.5 keV γ-rays, that have a short interaction length in germanium and produce spatially localized interactions. Figure 30 shows a single experimental pulse (black points), the average experimental pulse (dotted black line) and the simulated pulse (blue line). The noise fluctuations of the single pulse are greater than the differences between the simulation and the average experimental signal. The simulated pulse shapes show a good agreement with the experimental data for each measurements carried out so far. The slight deviations between the simulated and the average measured signals can be related to inaccuracies in the implementation of the detector properties[2].
The computation of the electron and hole trajectories inside the BEGe detector gave an important insight on the origin of the peculiar shapes of the BEGe detector signals and on their time dependence on the interaction position. Moreover, the calculation of the

[2]For instance, a small variation in the impurity distribution produces a significant modification of the simulated pulse shapes. In this work the manufacturer's information was used, which already provides fairly good results.

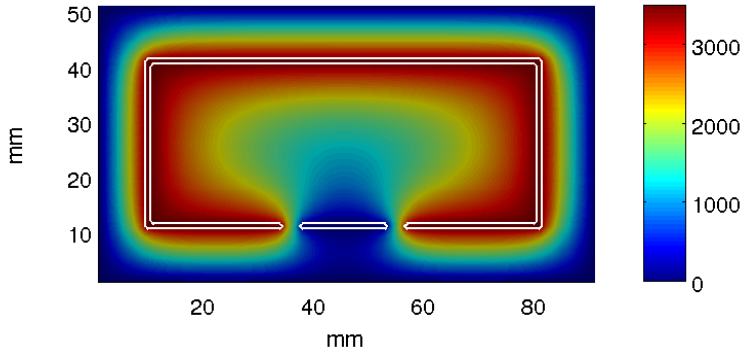

Figure 29: Electric potential expressed in Volt computed for a vertical section of the BEGe detector passing through the symmetry axis of the detector.

pulse shapes allowed the investigation of the pulse shape discrimination capabilities of this detector between SSE and MSE and possibly the tuning of the analysis algorithms.

9.2 New Energy Spectrum Toolkit

On a broader perspective, in the light of the future data taking, the development of a general "New Energy Spectrum Toolkit" (NEST) was started. NEST is meant to draw, scale, and stack simulated energy spectra (e.g. from MaGe) in order to assemble a realistic energy spectrum as measured in the early phase of the GERDA experiment. The final goal is to fit simulated energy spectra to a measured energy spectrum and to extract parameters, e.g. the radioactive contamination of a certain part used inside the GERDA experiment. A single set of parameters and a single list of spectrum contributions exists. A parameter is characterized by name, value unit and a description. The parameters are for example half-lives of isotopes and radioactive contaminations of materials. A spectrum contribution is characterized by type, parameter list, location of the output ROOT file (produced by Mage) containing the energy spectrum and further optional properties.
The toolkit is ROOT-based and uses the Extensible Markup Language (XML) in the parameters and spectrum-contribution list. First spectra with NEST have been already been assembled for testing and debugging purposes.

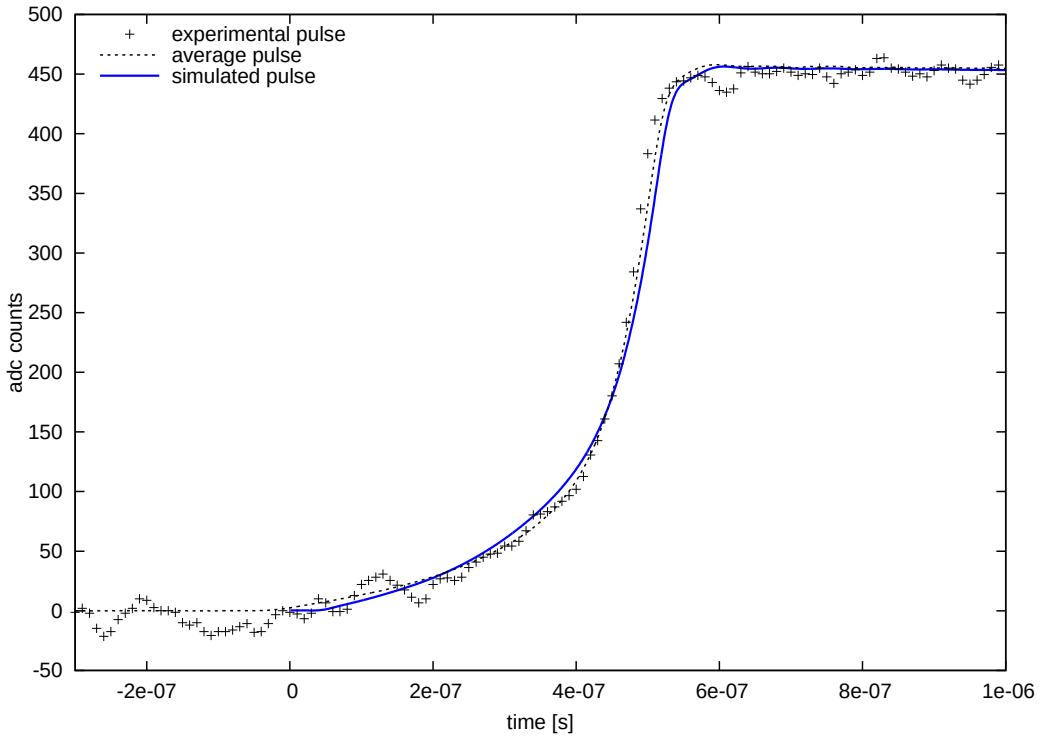

Figure 30: Comparison between an experimental pulse, the average experimental pulse and the simulated pulse. Data have been collected with a collimated ^{241}Am source placed on the top surface of the detector, 15 mm far from the center. The deviations of the simulated signal from the average signal are small as compared to the single event noise fluctuations.

10 Material screening

10.1 Radon emanation measurements

^{222}Rn emanation measurements were performed in order to quantify and (if necessary) to reduce the total ^{222}Rn emanation rate of the GERDA inner detector (lock and cryostat). During the last months several missing items were installed in order to prepare the cryostat for the LAr filling (see section 1): The manifold with its connection tubes, a compensator, the active cooling system, valves, safety equipment and several sensors. Moreover, a copper shroud was inserted to avoid the convection-driven radon transport from the outer parts of the cryostat towards the diodes.

After the installation another campaign of ^{222}Rn emanation tests of the cryostat was performed in September 2009. After filling the cryostat with ^{222}Rn-free nitrogen and

Sample description	**Single results [mBq]**	**Average [mBq]**	**Comments**
1^{st} test, SIMIC	$16.9 \pm 1.6_{stat} \pm 3.0_{sys}$		Cryostat after cleaning, No
Nov. 2007	$29.8 \pm 2.4_{stat} \pm 5.8_{sys}$	23.3 ± 3.6	mixing prior to extraction
2^{nd} test, SIMIC	$13.6 \pm 0.7_{stat} \pm 2.4_{sys}$		Cryostat after additional
GS, March 2008	$13.7 \pm 0.7_{stat} \pm 2.7_{sys}$	13.7 ± 1.9	cleaning
3^{rd} test, GS	$33.0 \pm 2.8_{stat} \pm 7.0_{sys}$		After copper shield
June 2008	$35.7 \pm 2.9_{stat} \pm 8.8_{sys}$	34.4 ± 6.0	mounting
	$33.2 \pm 3.5_{stat} \pm 1.9_{sys}$		After wiping of
4^{rd} test, GS	$31.3 \pm 4.6_{stat} \pm 3.4_{sys}$	30.6 ± 2.4	copper / steel surface
November 2008	$27.3 \pm 2.4_{stat} \pm 0.7_{sys}$		Precise pressure reading.
	$49.9 \pm 3.3_{stat} \pm 2.1_{sys}$		
5^{th} test	$63.8 \pm 4.1_{stat} \pm 3.1_{sys}$		After mounting of shroud
September 2009	$56.2 \pm 3.7_{stat} \pm 2.7_{sys}$	54.7 ± 3.5	manifold, compensator and
	$49.1 \pm 3.3_{stat} \pm 2.2_{sys}$		cryogenic tubing

Table 4: ^{222}Rn emanation from the GERDA cryostat at different preparation stages.

waiting for ≈ 10 days the gas was mixed (assuring homogeneous Rn distribution in the entire volume) and small samples (several m^3) were taken. Next, their ^{222}Rn concentration were measured and the results were scaled to the entire cryostat. The average result of 4 individual tests was (54.7 ± 3.5) mBq (saturation activity). This is about 25 mBq more than in the previous test indicating that the newly installed equipment has introduced new ^{222}Rn sources (see Table 4). Another test was performed without prior mixing. Its result is about twice as high as the other four tests indicating that a homogeneous distribution is not given without mixing. Because the sampling port is at the manifold, this is an indication for ^{222}Rn sources in the neck region of the cryostat. If confirmed this would be favourable, since the active cooling should provide a stable temperature gradient of the LAr in the neck region, thus avoiding a convective top-bottom ^{222}Rn transport.

It should be noted that all cryostat measurements are performed at room temperature while the cryostat will finally be kept at -186 C (liquid argon temperature). Therefore, we have started a program to investigate the ^{222}Rn emanation from a metal matrix at cryogenic temperatures. Preliminary results show that the environment is very important: If the emanation happens into a gaseous helium environment it is suppressed significantly at low temperatures. This seems not to be the case if the emanation happens into liquid argon. The observation might be explained as follows: In liquid argon the emanated ^{222}Rn stays dissolved, while in gaseous helium it has a higher mobility and arrives quickly at cold surfaces where it condensates. Further studies are underway to quantify the effect.

Beside the cryostat several other samples were screened for their ^{222}Rn emanation. The results are shown in Table 5. The shroud inside the cryostat is made out of a 30 μm copper

Sample	Emanation rate	Remarks
30 μm copper foil	< 134 μBq	Same amount as for shroud
Ullage tank	< 1.2 mBq	Cryostat gas buffer volume
Radon monitor	(0.47 ± 0.06) mBq	
PTFE-ring + ^{226}Ra	(12.9 ± 0.8) mBq	
PTFE-ring + ^{226}Ra aft. cleaning	(0.9 ± 0.2) mBq	Cleaned with acetone
Molecular sieve zeolite Z10	(2.1 ± 0.1) Bq/kg	At room temperature
Molecular sieve zeolite Z10	(2.6 ± 0.1) Bq/kg	At 200 °C
Molecular sieve zeolite Z4	(130 ± 10) mBq/kg	At room temperature
Polyurethane o-rings (93° Sh)	(40 ± 3) mBq/m^2	Diameter: 2mm and 3mm
Polyurethane o-rings (90° Sh)	< 1 mBq/m^2	Diameter: 4mm
LEDs	(52 ± 6) μBq/piece	For light in the lock
Aluminum foil	< 53 μBq/m^2	Standard household foil
10 % borated polyethylene	(440 ± 110) μBq/m^2	

Table 5: ^{222}Rn emanation rates of various samples.

foil. We have assayed a similar amount of this foil for ^{222}Rn emanation. The result shows that the contribution from the shroud is negligible. Also the ullage tank used to provide a buffer volume adds a negligible activity to the overall ^{222}Rn budget of the cryostat. An acetone cleaning efficiency was tested with a small PTFE ring which showed a high ^{222}Rn emanation rate before, probably because it was in contact with a ^{226}Ra solution. It could be reduced by a factor 14. The same cleaning procedure is also applied for the PTFE pieces in close neighbourhood to the enriched diodes. For polyurethane o-rings and zeolites significantly differences in emanation rates were discovered depending on the individual batch or microstructure. It is remarkable that the zeolite Z10 shows only a small increase of the ^{222}Rn emanation rate at elevated temperatures. During previous investigations of porous materials a much stronger dependence has been observed.

10.2 Radon monitoring

The electrostatic radon monitor which was discussed in previous progress reports was shipped to the Gran Sasso underground laboratory in August and successfully installed in September. Within the next months, it will be connected to the exhaust line of the GERDA cryostat to measure the radon content in the gaseous Ar. The foreseen flow of 6 litres per minute results in a gas exchange in the 711 litre vessel within 2 hours. Under this condition, the background of the radon monitor resulting from the emanation of the inner tank should stay below 15 μBq. This emanation background is sufficiently low for our estimated detection limit of about 70 μBq corresponding to about two extra counts per day.

The Labview software calculates the Radon concentration based on the ^{214}Po and ^{218}Po

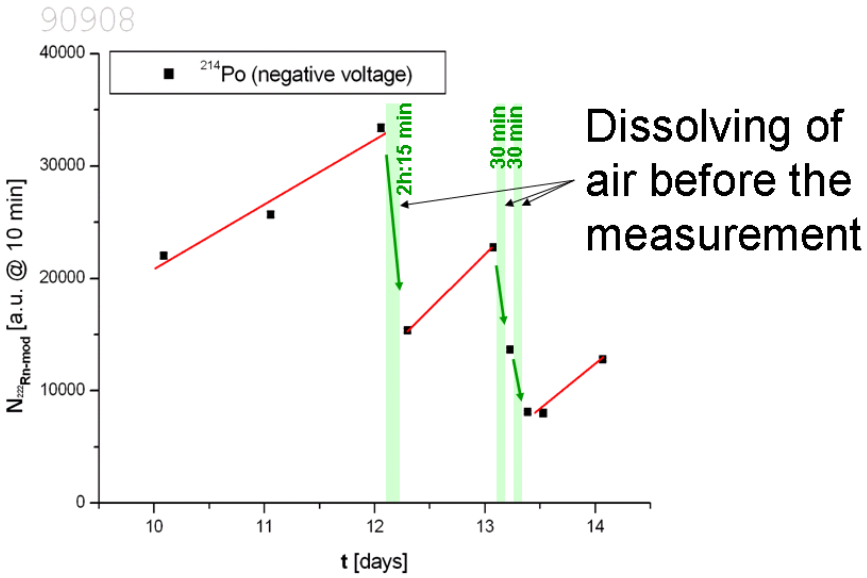

Figure 31: Influence of impurities on ^{214}Po collection

peak intensity, the Radon detector geometry as well as the calibration data and writes the last two measured Radon concentrations in a file from which the data can be read by the GERDA slow control. The measurement of the last month shows an emanation of the closed detector steel Vessel including the inlet system of (0.3 ± 0.1) mBq. This has to be compared to the result of an emanation measurement using proportional counters (0.46 ± 0.06) mBq, see section 10.1).

10.3 Behaviour of radon in liquid and gaseous nitrogen

Influence of impurities in LN_2 According to the recent report (LNGS-EXP 33/05 add. 8/09, Appendix, par. 12.3) the influence of impurities present in LN_2 on Rn daughters transport therein was investigated. A decrease in the amount of collected ^{214}Po atoms on the steel plates put on some potential was clearly seen after dissolving of air in liquid nitrogen. Fig. 31 presents the results.

Radon atoms are neutral while dissolved in LN_2. Their decays with release of high energy alpha-particles result in initially highly charged atoms of ^{218}Po, caused by recoil energy of the alpha-decay. After thermalization atoms still have a fair chance of being charged. Neutralization by charge transfer is forbidden due to differences in ionizing energies between ions and the surrounding nitrogen (or argon) atoms. Beta-decay produces ions in +1 charge state.

The ions have however a chance to be neutralized by interaction with impurities possessing lower ionizing potential or with free electrons. They also may form bigger clusters with impurities. Therefore the fraction of ions retaining their charge is mainly related to

# of counts	in gas		in liquid	
	^{218}Po	^{214}Po	^{218}Po	^{214}Po
No HV	9±3	22±5	0	0
+2 kV	5±3	23±5	0	13±4
–2 kV	536±23	2717±52	1±1	44±7

Table 6: Alpha count numbers for measurements in gaseous and liquid nitrogen after radon dissolving in gaseous nitrogen

the concentration of impurities in the environment.

The growth in time of number of charged Rn daughters in a medium (LN_2/LAr) may be related to decreasing concentration of impurities caused e.g. freeze out or sedimentation. As a result more ions retain their charge and e.g. may be transported to the ion collector by the electric field (like Stainless Steel Plates or bare detectors being put on HV).

^{222}Rn in the gaseous nitrogen ^{222}Rn has been ad-mixed to the nitrogen gas present above the Rn-free LN_2 filled into a 20-l dewar. Several tests have been performed in order to check how the radon atoms will behave, also with respect to the transfer into the liquid phase. To do so Stainless Steel Plates (SSPs) kept on HV were placed for 3 h above the surface of LN_2. They collected the daughters of the decaying Rn and gave indication of its activity. Table 6 presents the results of the measurements carried out at various conditions like positive, negative and no HV applied to the SSP.

The high number of ions collected on a SSP put on negative HV is meaningful. The estimated volume above the LN_2 surface was about 15 l. Due to the high flow rate of boil-off nitrogen thes volume can be cleaned in a short time after introducing radon (boil-off production rate is about 60 l/h). Consequently, the only origin of ions could be the cold walls of the dewar. While introducing in the gaseous phase, radon atoms quickly froze out on there while the rest was flushed out by boil off gas. Decays of radon on the walls produced positive ions that were attracted after thermalization by the negative HV to the surface of the SSP.

Relatively low concentration of impurities in boil-off nitrogen prevents positive ions from forming bigger clusters with negatively charged impurities, serving as carriers for ions in positive HV. For this reason positive HV collected much lower number of ions.

The SSPs were also immersed in LN_2 and supplied with high voltage. The amounts of collected ions on negative, positive and no HV were much lower compared to the gas phase results, however the results show that a certain amount of Rn was transferred from the gas to the liquid phase of nitrogan.

Conclusions Inlet of radon atoms from the lock system is less severe due to direct freezing out on the cold surfaces. It is clear that SSP placed on negative potential attracts radon progenies in the gas phase much more efficiently than positive, as it is expected.

10.4 Gamma ray screening

The gamma ray screening tests with low background Germanium detectors were mainly focused on front-end electronics (see Table 7). A full PCB showed rather high concentrations in ^{226}Ra, although the substrate (Cuflon) which makes up the major mass fraction of the PCB is very pure. Since the used solder was found to be pure as well, the source of contamination was expected to be in the remaining components (FETs, resistors, capacitors), although they have a tiny mass. To identify and replace the problematic elements, the components were removed from the substrate and screened individually. As can be clearly seen from Table 7 the capacitors were responsible for the relatively high ^{226}Ra level in the PCB. This can be understood, because they contain barium which is chemically similar to radium. To overcome this problem we exchanged them by barium-free tantalum capacitors. Indeed the screening revealed that they are much cleaner than the Ba-capacitors. Finally a screening of the modified PCB has shown that the ^{226}Ra contamination could be reduced by more than a factor 10. The achieved purity levels are sufficient for phase I of GERDA.

Sample	**Massic activities [mBq/kg]**			
	^{226}**Ra**	^{228}**Th**	^{228}**Ra**	^{40}**K**
PCB	970 ± 10	29 ± 13	32 ± 19	340 ± 110
Cuflon (Polyflon)	< 0.79	< 1.8	< 2.7	43 ± 13
SMD FETs	640 ± 160	690 ± 180	< 540	< 2600
SMD resistors	< 670	< 630	< 620	< 6300
Ba capacitors NP0	18000 ± 5000	< 11000	20000 ± 10000	< 9800
Ba capacitors X5R	29000 ± 3000	7000 ± 1000	< 7600	< 22000
Ba capacitors X7R	42000 ± 6000	15000 ± 4000	< 15000	< 29000
Ta capacitors 10 μF	< 570	1300 ± 400	< 1700	13000 ± 5000
Ta capacitors 4.7 μF	< 380	500 ± 200	< 920	17000 ± 4000
Modified PCB	78 ± 16	< 45	< 31	600 ± 210

Table 7: Gamma ray screening results of the GERDA front-end cirucit and various components.

10.5 Neutron activation of materials relevant for GERDA

For a good simulation of the GERDA detector we need to know the exact activity of the components of the detector. The activities of the construction materials are caused by impurities or induced by activation due to cosmic rays. We want to investigate the activation by cosmic neutrons.

G. Heusser and M. Laubenstein measured the activity of copper and stainless steel irradiated by cosmic rays. The comparison with determined activities shows some deviations between calculation and experiment. We also try to determine the activations of

stainless-steel and copper. By studing the input parameters for the calculations we found big influences of the different neutron spectra by changing the surrounding matter. We also found that the terrestrial neutron spectra is poorly known; there are only data from two valid measurements.

At the "Forschungszentrum Dresden Rossendorf", we want to measure some cross sections to tune the calculations. The facility provides the 14 MeV D-T neutron generator of the TU-Dresden. We practiced methods for measuring cross sections for neutron energies around 14 MeV. Therefore we studied different reactions like ^{54}Fe(n,p)^{54}Mn, or ^{65}Cu(n,α)^{62}Co. The reaction ^{27}Al(n,α)^{24}Na is used to monitor the neutron flux. For the determination of the neutron energy we use the niobium-zirconium method. The method uses the well known cross sections of the reactions ^{90}Zr(n,2n)$^{89g+89m}$Zr and ^{93}Nb(n,2n)^{92m}Nb. It is also a good method for monitoring the neutron flux.

To measure cross sections for reactions to short living activation products we developed a powerful pneumatic delivery system. It should be installed until the end of 2009. The system provides two buffers for samples and a fast allocator. A USB I/O System controls the valves, the light barriers and the servo motors. Thus we reach short delays between irradiation and measurement.

The neutron cross sections at higher energies are also poorly known. At a different facility we are measuring cross sections at higher neutron energies.

References

[1] M. Knapp, PhD thesis 2009, Eberhard Karls Universität Tübingen

[2] See http://www.canberra.com/products/485.asp

[3] D. Budjas *et al.*, JINST **4** (2009) P10007

[4] I. Abt *et al.*, Nucl. Instr. Methods A **570** (2007) 479

[5] L. Mihailescu *et al.*, Nucl. Inst. and Meth. A **447** (2000) 350

[6] B. Bruyneel *et al.*, Nucl. Inst. and Meth. A **569** (2006) 764

[7] P. Medina *et al.*, IEEE IMTC (2004).